ACTA METALLURGICA SLOVACA
2021, VOL. 27, NO. 1, 4-10

RESEARCH PAPER

EXPERIMENTAL STUDY ON THE MECHANICAL BEHAVIOUR OF FIRED SAND-CLAY AND GLASS POWDER-CLAY BRICKS

Adeolu Adesoji Adediran[1,3]*, Abayomi Adewale Akinwande[2], Oluwatosin Abiodun Balogun[2], Olanrewaju Seun Adesina[1], Adeniyi Olayanju[3]

[1] Department of Mechanical Engineering, Landmark University, PMB 1001, Omu-Aran, Kwara State, Nigeria.

[2] Department of Metallurgical and Materials Engineering, Federal University of Technology, Akure, PMB 704, Ondo State, Nigeria.

[3] Landmark University SDG 9 (Industry, Innovation and Infrastructure Research Group), Landmark University, PMB 1001, Omu-Aran, Kwara State, Nigeria.

*Corresponding author: adediran.adeolu@lmu.edu.ng,dladesoji@gmail.com tel.: +234-803-245-8545, Department of Mechanical Engineering, Landmark University, PMB 1001, Omu-Aran, Kwara State, Nigeria.

Received: 30.07.2020
Accepted: 12.10.2020

ABSTRACT

Mechanical behaviour of fired bricks containing varied amount of fine sand (FS) and waste glass powder (GP) was investigated. FS and GP were added to bricks at varied amount of 0, 5, 10, 15, 20, 25, 30, 35 and 40 wt. %. Firing was done at 1200 °C and samples produced were evaluated for compressive and flexural strengths while microstructural analyses of 25 wt. % FS and GP-clay bricks were examined. Results showed that compressive strength was highest at 30 wt. % GP for GP-bricks while for FS-clay bricks, compressive strength rose to 11.4 and 12.8, at 35 and 40 wt. % FS addition. Flexural strength for GP-clay and FS-clay bricks peaked at 30 wt. % GP (3.63 MPa) and 40 wt. % FS (2.45) respectively. Flexural modulus increased progressively and exponentially as FS and GP proportion increased. Work done in resisting deformation and deflection during bending reduced with increased amount in both additives. Flexural strain was inversely related to load and stiffness. In conclusion, addition of GP and FS in increasing amount resulted in improved mechanical properties in the bricks. Also, increased proportion of GP and FS was found to improve response to loading in fired bricks.

Keywords: glass; sand; fired bricks; mechanical properties

INTRODUCTION

Ceramics are inorganic materials made of metal and non-metal compounds and are composed of silica, alumina, magnesia, zirconia, and other compounds. Properties of these materials include resistance to corrosion and chemical attack due to their inert nature, poor conduction of heat and electricity and high compressive strength. They are also hard, brittle and heavy with poor tensile properties [1-3]. Fired clay are ceramics which are made hard by firing, while unfired clay ceramics are made hard by sun drying or oven drying. Concrete or cement bricks are a form of ceramic products which are made strong by the addition of cement followed by further curing [4]. Oven drying is done on green ceramic body at 110 °C for water removal and decomposition of some organic elements present. Firing process involves exposure of ceramic body to high temperature for a period of time to enhance hardness, strength and other properties [5-7]. The process of sintering enhances bond within particles leading to improved properties [8]. Firing of clay is undergone in the production of potteries, wares, roof tiles and bricks. Properties of fired bricks include porosity, shrinkage, density, and strength. Clay in its raw form is porous which affects strength and density in the sense that higher porosity leads to reduced strength [7, 9]. For structural application, reduced porosity in bricks is necessary in order to ensure structural integrity of buildings. Reduced porosity in bricks results in reduced inter particle distance leading to enhanced bond between particles [10]. The process of reducing porosity in fired clay body involves the incorporation of additives like waste glass powder/shavings, eggshell powder, silica nano particles [11] and other additives. Adding of eggshell as biofillers to fired clay bricks [12] was noted to produce fired bricks of high compressive strength and hardness, good thermal expansion coefficient and lower water absorption at 25 wt. % eggshell powder addition. Addition of waste glass, was recorded to reduce porosity and water absorption while increased compressive strength was noted, when waste glass powder was added in increasing proportion of 0, 10, 20, 30, and 40 wt.% [13,14]. In this study, waste glass powder and fine sand were added to fired bricks and comparison was made on mechanical behaviour of such bricks at varied proportion addition; for application in masonry.

MATERIAL AND METHODS

Materials Preparation

Materials used include sand, glass bottles and clay. The sand was obtained from a stream; washed and sun dried for 3 days. Clay used was excavated from a depth of 1.5 m in a borrow pit in Aule, Ondo State, Nigeria. Water was added to the clay, stirred and left undisturbed for two days. The water was poured off leaving behind the clay. Fresh water was added, stirred and left undisturbed for another two days and the water was poured off while the left over clay was spread in a cotton material and allowed to sun dry for 7 days. Dried clay lumps were broken into smaller pieces, followed by crushing and milling. Waste

DOI: 10.36547/ams.27.1.622

glass bottles (bottles of soft drinks and alcoholic drinks) were bought from a shop where waste glass products were sold for recycling. The bottles were washed and sun dried for one day followed by crushing and milling before sieving. The sand, waste glass and milled clay were sieved using an electric sieve shaker (Model RX 29) which top sieve has an aperture of 4750 µm. Clay (sieved to 300 µm), glass powder (GP) and fine sand (FS) which were sieved to -150 µm were collected and used for sample preparation.

Sample Preparation

Two groups of samples were prepared: fine sand-clay (FS-clay bricks) samples and glass powder-clay (GP-clay bricks) samples. FS-clay brick samples contained sand at varying proportion of 0, 5, 10, 15, 20, 25, 30, 35 and 40 wt. % of fine sand while GP-clay bricks samples contained the same varying proportion of GP (Table 1). Clay was mixed with water and the additives in a mechanical mixer and the slurry moulded into shape using compression moulding machine at 10 MPa. Water was added during mixture at water to clay ratio of 7:20. The green bricks produced were left undisturbed for 24 hours after which they were oven dried for 12 hours at a temperature of 110 ^{o}C in order to remove moisture and other volatile content. This was followed by firing in an electric furnace at 5 ^{o}C/min until 1200 ^{o}C was attained. The temperature was maintained for 4 hours before allowing samples to cool to room temperature in the furnace. Bricks 150 mm × 150 mm × 150 mm and 400 mm x 100 mm x 100 mm were produced for this study.

Table 1 Composition of samples

FS/GP	0	5	10	15	20	25	30	35	40
Clay	100	95	90	85	80	75	70	65	60

Preliminary test on materials used

Tests were carried out to examine the specific gravity, bulk density and moisture content of sand and clay (in as received condition) as well as glass powder (after sieving) in line with existing procedure stated in Table 2. Sieving was done out on the materials used as per [15,16]. Also, chemical composition of the materials were analysed and the results presented in Table 4.

Tests on brick samples

Compressive strength

Compressive strength test was carried out on each sample to determine its load bearing capacity in line with [17] procedure. The brick samples (150 mm × 150 mm × 150 mm) were initially oven dried at 110 ^{o}C until a constant mass was attained and tested using a universal testing machine (TBTUTM-600). The samples were placed flat horizontally between the plates of the machine and a load of 10 kg/min was applied. The maximum load at failure was recorded and the compressive strength calculated using the expression in Equation 1.

$$\text{Compressive strength (MPa)} = \frac{\text{Maximum load at fracture}}{\text{Cross sectional area}} \quad (1.)$$

Flexural strength

This strength evaluates the ability of bricks to resist deformation by bending and was carried out on samples (400 mm x 100 mm x 100 mm) immediately after cooling to room temperature. The test was done in line with [18] with a loading rate of 15 kg/min and the result evaluated using Equation (2).

$$\text{Flexural strength (MPa)} = 3Fh/2bd^2 \quad (2.)$$

Where F is the maximum load at fracture, h is the length of the support plan/length between supports; b is the width of the sample, d is the thickness/depth of the sample.

RESULTS AND DISCUSSION

Physical properties and chemical composition

Table 2 showed the physical properties of materials used which was in consistent with works reported by [19-21].

Table 2 Physical Properties of Materials Used

Properties	GP	FS	Clay
Specific gravity	2.75	2.67	2.61
Bulk density	2.01 g/cm^3	1.73 g/cm^3	1.58 g/cm^3
Moisture Content	-	4.2%	26.2%
Fineness Modulus	1.27	1.65	1.67

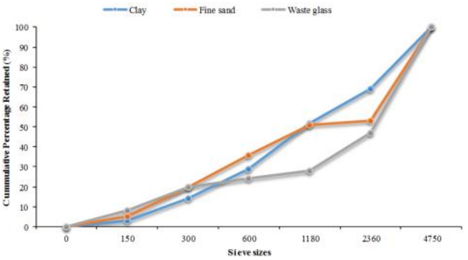

Fig. 1 Particle size distribution of GP, FS and Clay

Table 3 Chemical Composition of materials used (X-ray Fluorescence result)

Constituents	GP (%)	FS (%)	Clay (%)
SiO_2	71.8	78.3	60.1
Al_2O_3	2.5	8.8	25.1
Fe_2O_3	0.9	1.4	7.4
CaO	10.3	2.3	1.1
MgO	2.7	0.2	1.3
Na_2O	6.8	3.3	0.6
Others	3.6	3.0	0.3
Loss on ignition	1.4	2.7	4.1

The specific gravity of GP, FS and Clay used were evaluated to be 2.75, 2.67, and 2.61 respectively while bulk density was obtained as 2.01g/cm^3, 1.73 g/cm^3 and 1.58 g/cm^3. Results of the moisture content showed that clay in its raw state had moisture content of 26.2 wt. %, while fine sand had 4.2 wt. % moisture content. The finest of the materials was GP which had modulus of 1.27 falling in grading zone 2 as per [19]. From the results of the particle size distribution, 68.7 wt. % of GP lie below 300 µm sieve fraction. Based on the result on fineness modulus for FS (Fineness modulus of 1.65), FS falls under the classification of fine sand as per [19]. FS can be classified under grade 2 sand [20] indicating moderate fineness. 45.2 wt. % of the sand was retained below 150 µm. Clay has fine modulus of 1.75, with 46.3 wt. % retained on 150 µm. Table 3 highlights the chemical composition of materials used. Silica content is higher in the materials and from evaluation made 70% of the mix materials has silica content.

Analysis of mechanical behaviour of bricks

Compressive strength of brick samples

The plot showing the effect of compositions on compressive strength of samples is as shown in Fig. 2.

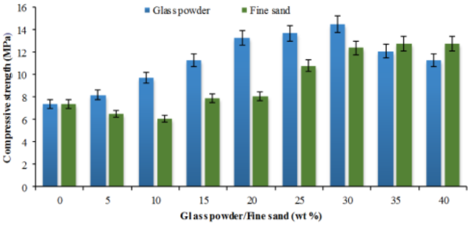

Fig. 2 Effect of compositions on compressive strength of samples

Compressive strength reduced from 7.4 MPa at 0 wt. % FS addition to 6.5 MPa at 5 wt. % FS addition (Fig. 2). It further reduced to 6.1 MPa at 10 wt. % addition which may be due to lower level of bonding between particles. This may be attributed to the lower adhesion between sand and clay particles due to the loose non plastic nature of sand (loose nature) and inability of sand to meet up with initial adequate bonding volume (Vi) for additives in the bricks, leading to lower level of compaction. At ≥15 wt. % FS addition, compressive strength increased progressively. At 25 wt. % content of FS, compressive strength increased by 33.3% to 10.8 MPa, and with further addition, it increased by 14.81% at 30 wt. % content of FS. The value remained constant at 35 and 40 wt. % addition but with reduced increment of 3.2%. Addition of ≥15 wt. % FS to clay resulted in enhancement of compressive strengths owing to ability of sand particles to fill in pores resulting in enhanced fusion and compactment.

At 5 wt. % glass powder (GP) addition, compressive strength rose to 8.2 MPa. As GP proportion increased, compressive strength increased further due to enhanced cohesion and compactment within the clay body. In addition, increased glass phase formed, further compliment the strong bond achieved thereby leading to increase in compressive strength. Compressive strength got to a peak of 14.5 MPa at 30 wt. % GP before declining at 35 wt. % and 40 wt. %. The results obtained in this present study can be compared with results recorded in [13,15] and [22] in terms of proportion of waste glass where maximum compressive strength was attained. According to [15] where 900 °C was employed in firing, maximum compressive strength was attained at 50 wt. % waste glass powder addition, though in present study, maximum strength was recorded at 30 wt. % GP. Authors [23] reported on fired clay samples at 1100 °C and a maximum compressive strength was recorded at 40 wt. % added content of milled glass (sieved to -100 µm) and further addition resulted in reduced strength. However, report from [13] attained maximum compressive strength at 1000 °C for 40 wt. % of waste glass (sieved to -150 µm) while at 1100 °C, maximum compressive strength was attained at 30 wt. % addition of waste glass. Further increase in waste glass content resulted in reduction in compressive strength. As waste glass proportion increased in the samples, there was increased glassy phase. However, as this glass phases expands, brittleness increased [13]. This explains the reduction in compressive strength beyond some certain proportion of waste glass addition. It can be deduced that when attaining ≥30 wt. % of waste glass powder, compressive strength reduces, though depends on firing temperature and sieve fraction of glass powder.

Flexural strength

Representative plot showing the effect of compositions on flexural strength of samples is shown in Fig 3.

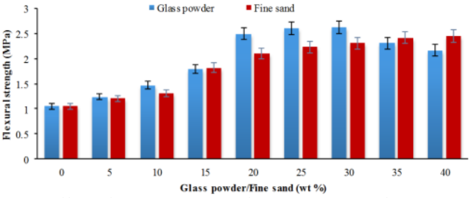

Fig. 3 Effect of compositions on flexural strength of samples

From Fig. 3, flexural strength increased progressively from 1.05 MPa at 0 wt. % of FS addition to 2.45 MPa at 35 and 40 wt. % of FS due to strong bond between sand-clay particles as a result of enhanced fusion. For samples with GP addition, flexural strength climaxed at 30 wt. % GP (2.63 MPa) and at further addition of GP, the strength declined in value due to the brittle glassy nature exhibited in bricks. Samples containing between 20 to 40 wt. % of both sand and glass powder met standard [24,25] for masonry bricks.

Flexural modulus and strain

Further analysis involves evaluation of flexural modulus. The deflection exhibited during the test for flexural strength was measured and recorded and the flexural strain evaluated using Equation (3).

$$\text{Flexural strain } (\alpha) = 6dt/L^2 \qquad (3.)$$

Where d was the recorded deflection (mm), t was thickness of sample and L is the distance between two supports. Flexural Modulus (GPa) was evaluated as flexural strength divided by flexural strain, while work done in resisting deformation during deflection (Nm) was evaluated by multiplying maximum load at failure (N) by deflection (mm).

Table 4 shows the average deflection, work done and flexural Modulus for Fine Sand (FS). Table 5 shows the average deflection, work done and flexural Modulus for Glass Powder (GP).

Table 4 Average deflection, work done and flexural Modulus for Fine Sand (FS)

Fine sand (wt. %)	Maximum load at Failure (N)	Average deflection (mm)	Flexural Strength (FS) (MPa)	Flexural Stiffness (x 10^{-3} N/m)	Flexural strain (α)	Work done (x 10^{-3} Nm)	Flexural Modulus (GPa)
0	17.96	0.80	1.05	22.45	0.0120	14.37	0.0875
5	20.69	0.62	1.21	33.37	0.0093	12.83	0.1300
10	22.40	0.44	1.31	50.90	0.0066	9.86	0.1985
15	31.12	0.35	1.82	88.91	0.0053	10.90	0.3434
20	35.91	0.31	2.10	115.84	0.0047	11.13	0.4468
25	38.13	0.22	2.23	173.32	0.0033	8.39	0.6758
30	39.50	0.14	2.31	282.14	0.0021	5.53	1.1000
35	41.38	0.09	2.42	459.78	0.0014	3.72	1.7285
40	41.90	0.07	2.45	598.57	0.0011	2.93	2.2273

Table 5 Average deflection, work done and flexural Modulus for Glass Powder (GP)

Glass Powder (wt. %)	Maximum Load at Failure (N)	Average deflection (mm)	Flexural Strength (FS) (MPa)	Flexural Stiffness (x 10^{-3} N/m)	Flexural strain (α)	Work done (x 10^{-3} Nm)	Flexural Modulus (GPa)
0	17.96	0.71	1.05	25.30	0.0110	12.75	0.0955
5	21.20	0.54	1.24	39.26	0.0081	11.45	0.1296
10	25.14	0.42	1.47	59.86	0.0063	10.56	0.2333
15	30.61	0.28	1.79	109.32	0.0041	8.57	0.4366
20	42.75	0.22	2.50	194.32	0.0033	9.41	0.7576
25	44.63	0.12	2.61	371.92	0.0018	5.36	1.4500
30	44.97	0.06	2.63	749.50	0.0009	2.70	2.9222
35	39.50	0.04	2.31	987.50	0.0006	1.58	3.8500
40	37.11	0.03	2.17	1237.00	0.0004	1.11	5.4250

Effects of composition on flexural modulus and flexural stiffness of samples

Representative trend showing variations in Flexural modulus Fig 4(a) and flexural stiffness Fig 4(b) at increasing Glass powder and Fine sand content.

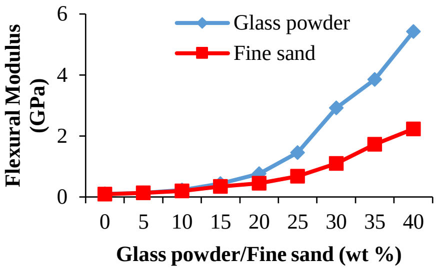

Fig. 4 (a) Showing Flexural modulus

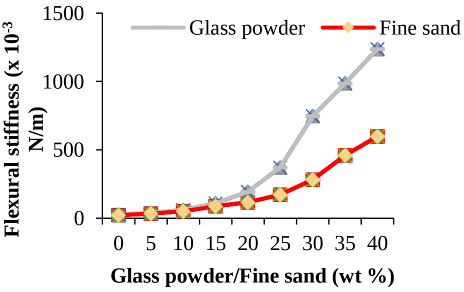

Fig.4 (b) Showing Flexural stiffness

As glass powder and sand content increased, flexural modulus increased (Fig. 4a), average deflection decreased leading to continuous decrease in strain. This resulted into progressive increase in flexural modulus, indicating increase in stiffness as glass powder and sand content amount increased. The strong bond formed between particles of clay and fine sand amounted to increased stiffness and rigidity. Increased compactment and strong adhesion between GP-clay bricks particles further enhanced resistance to bending in samples with GP. The strong glassy phase formed in samples containing GP further enhanced the resistance to deflection in GP-clay bricks samples, leading to high degree of flexural modulus compared with FS-clay samples. Flexural moduli for both samples (GP-clay and FS-clay bricks) were almost the same from 0 wt. % of to 15 wt. % addition of the additives. However, at 20% addition, the difference was becoming clearer. Between 20 wt. % and 25 wt. % addition of GP, there was a large increment of almost 91% in flexural modulus of GP-clay bricks compared to 51% in FS-clay bricks. As the content of the additives increased to 30, 35 and 40 wt. %, progressive increase in flexural modulus was 101%, 32% and 41% respectively for GP-Clay bricks, while in the case of FS-clay bricks, the progressive increase was 62%, 32% and 26% respectively. The flexural modulus- curve was exponential and progressive for GP-clay bricks and FS-clay bricks. Percentage increment of flexural modulus, in GP-clay was much higher than that of FS-sand, as a result of increased strong glass phase formed in the samples as GP content increased, which further complemented the bond formed between GP and clay particles. From the Fig. 4a, addition of ≥ 25% of both additives resulted in significant resistance to bending in bricks. Flexural stiffness (Fig. 4b) also followed the same trend for both FS and GP-clay bricks in that at 20 wt. % content of the additives, stiffness increased exponentially.

Effect of composition on work done during bending

Fig. 5 shows the downward movement of the work done in resisting deflection at maximum load application for both GP-clay and FS-clay bricks. This is attributed to increased resistance to deflection in the samples as content of both GP and FS were increasing. The additives were effective in the reduction of work done in resisting deflection. Work done in GP-clay bricks is lower than that of FS-clay bricks except at 10 wt. % of the additives where it's vice versa. This implies that as additives increased in the sample, the work done against load applied in causing deflection reduced, indicating high resistance to deflection. Comparing the two forms of bricks, work done against load in GP-clay bricks is lower than that of FS-clay bricks for each mix proportion (except for 10 wt. %), indicating, there is higher resistance to load in GP-clay bricks than in FS-clay bricks.

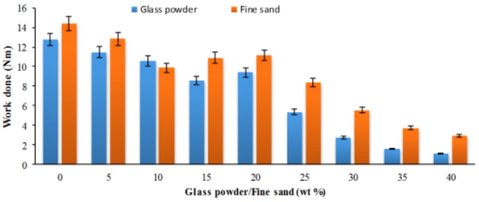

Fig. 5 Variation in work done in bricks during bending test

Flexural strain against maximum load at failure for brick samples

The strain-load curve in Fig. 6(a) shows the decrease in strain at failure as maximum load increased. For load between 18 N and 42 N, the strain ranged between 0.004 and 0.011 for FS-clay bricks. At higher FS proportion of ≥ 25 wt. %, increment in load applied was lower compared to compositions below 30 wt. % which also resulted into lower reduction in strain experienced at ≥ 25 wt. % FS addition owing to increased compactment in the samples. As load applied lied between 17 and 45 N, strain at failure was reducing (Fig. 6(b)). There was a 20% reduction in strain between 15 wt. % of GP and 20 wt. % of GP with a corresponding 4.4% increase in load to failure. At ≥ 20 wt. % GP, there was shrinkage in strain which resulted into corresponding lower percentage increase in maximum load to fracture for samples.

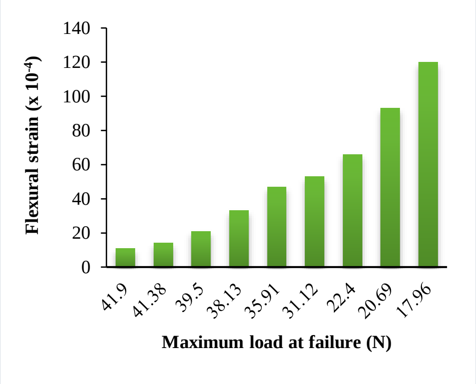

Fig. 6 (a) Plot showing the curve of strain at failure against maximum load at failure for FS-clay bricks

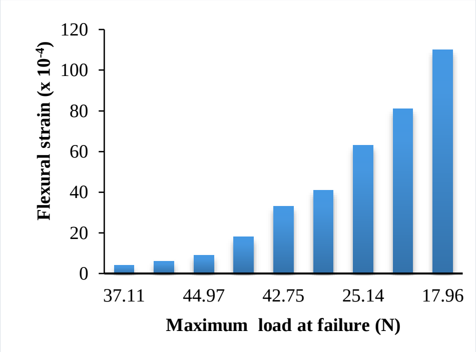

Fig. 6 (b) Plot showing the curve of strain at failure against maximum load at failure for GP-clay bricks

Generally, with increased load, strain at fracture reduced for both forms of bricks, due to reduced work done in resisting deflection as FS and GP contents increased in the samples. In Fig. 6b, highest load was recorded at 30 wt. % of GP with a resulting strain of 0.009. At 35 and 40 wt. % of GP, strain further reduced to 0.006 and 0.004 respectively, which was a further reduction of 33.3 and 55.6 % respectively, owing to higher value of stiffness.

Flexural strain against stiffness for brick samples

The representative plots showing the flexural strain against flexural stiffness for FS-clay bricks and GP bricks are as shown in Fig. 7 (a) and (b) respectively.

From Fig. 7 (a) and (b), flexural strain reduced with increased stiffness for both type of bricks. This is due to increased strength induced as composition of FS and GP increased in samples. Flexural strain was higher in FS-clay bricks than GP-clay bricks, while flexural stiffness was higher in GP-bricks than FS bricks. This can be attributed to the fineness of GP, with fineness modulus of 1.50, which is lower than that of sand (fineness modulus of 2.26). A finer particle of additive contributes to strength improvement in bricks [13].

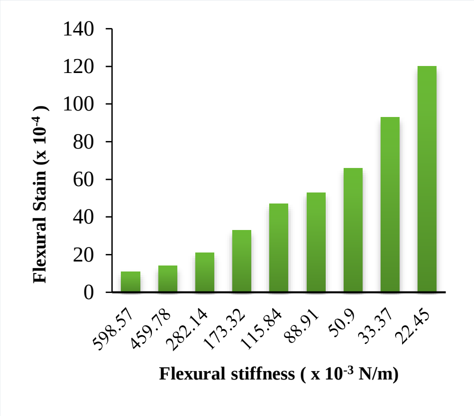

Fig. 7 (a) Plot of flexural strain against flexural stiffness for FS-clay bricks

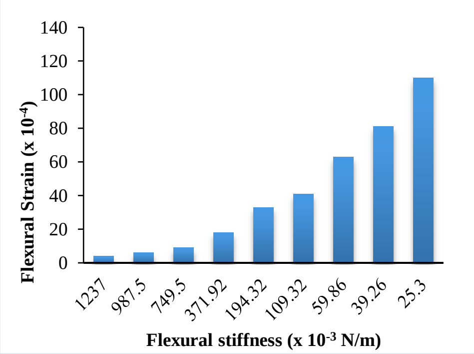

Fig. 7 (b) Plot of flexural strain against flexural stiffness for GP-clay bricks

Microstructural response

The representative morphological images for samples at 0 wt.% FS/GP, 25 wt.% FS and 25 wt.% GP are as shown in Fig. 8(a), (b) and (c) respectively.

Fig 8 (a) highlights the SEM image of brick sample with 0% GP/FS addition. Large amount of pores are observed when compared with bricks containing FS and GP. This explains the reason for lower compressive and flexural strength in sample with 0% GP/FS-clay bricks when compared with 25 wt. % FS-clay bricks and 25 wt. % GP-clay bricks. Fig. 8(b) shows image of 25 wt. % of FS-Clay bricks with few pores present. The sand particles infused into the clay leading to reduction of pores. This explains reason for higher strength in FS-bricks when compared with 0 wt. % GP/FS sample. In the case of 25 wt. % GP addition (Fig. 8c), porosity reduced and there is presence of glass luster as a result of glassy phase formed. The bond between GP and clay particles and the strong glassy phase resulted into improved and higher strength in GP-bricks than FS-bricks.

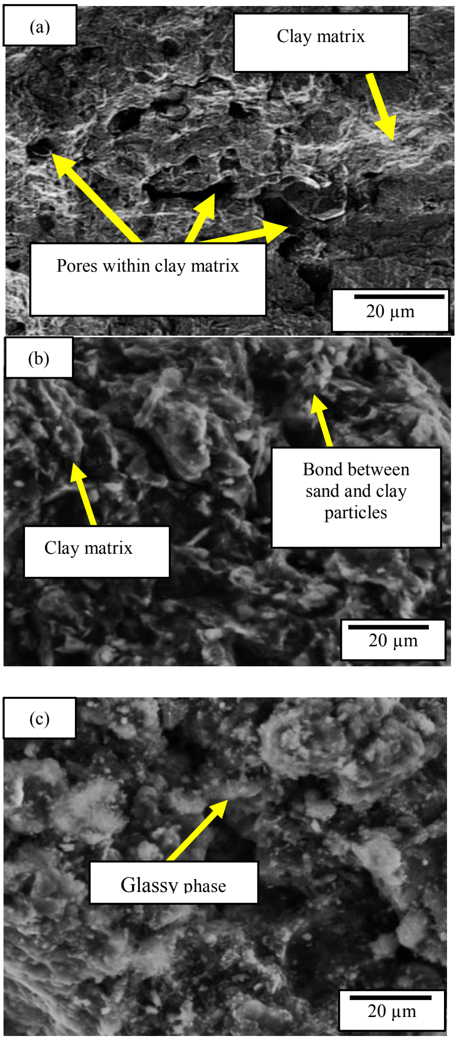

Fig. 8 Showing the SEM images of samples at (a) 0 wt.% FS/GP (b) 25 wt.% FS (c) 25 wt.% GP

CONCLUSIONS

Fine sand and glass powder were added to fired bricks at varied proportion of 5 wt. % to 40 wt. %, and it was concluded that the incorporation of the two additives enhanced the compressive and flexural strengths, and mechanical response to loading. Addition of glass powder up to 30 wt. % gave maximum compressive and flexural strengths; further addition may result in reduction in the strengths. Addition of fine sand sieved to - 150 μm at ≥ 15 wt. %, improved mechanical properties of fired bricks at increased proportion. Therefore, addition of glass powder and sand can improve properties of fired bricks for structural application, though glass powder proved to be more effective.

ACKNOWLEDGMENTS

Authors are grateful for the support from Landmark University Centre for Research, Innovation and Discoveries (LUCRID) through Industry, Innovation and Infrastructures, SDGs 9 Group.

REFERENCES

1. Q. Fang, P. S. Sidky, M. G. Hocking: Corrosion Science. 39(3), 1997, 511-527. https://doi.org/10.1016/S0010-938X(97)86100-8.
2. R. Bermejo, R. Danzer: Materials Science and Engineering Materials. 2, 2014, 285-298, https://doi.org/10.1016/B978-0-08-096527-7.00028-3.
3. F.O. Aramide, O.D. Adepoju, A.A. Adediran, A. P. Popoola: Cogent Engineering, 6(1), 2019, 1584938. https://doi.org/10.1080/23311916.2019.1584938.
4. A. Hafez, M.M.A. Khedr, M. Mohammed, R. Osman, R.M. Sabry: Journal of Engineering and Applied Sciences, 12, 2017, 2854-2862.
5. P.R. Fernando, G. L. Kannangara, G.P. Buddhika, A. Urushiya: Engineering Physics, 2(1), 2018, 15-22, https://doi.org/10.11648/j.ep.20180201.14.
6. O. A. Balogun, A. A. Akinwande, A. A. Adediran, P. P. Ikubanni, S. A. Shittu, O.S. Adesina: Journal of Materials in Civil Engineering, https://doi.org/10.1061/(ASCE)MT.1943-5533.0003532. (in press).
7. A. A. Akinwande et al.: Acta Metallurgica Slovaca, 26(3), 2020, 84-94, https://doi.org/10.36547/ams.26.3.605.
8. J. Izwan, S. Said, B. Abu, B.H. Bakar, A. Zainal: Science of Sintering, 42, 2010, https://doi.org/10.2298/SOS1002245J.
9. P. Velasco, M.P. Morales, M.A. Giró, L. Velasco: Construction and Building Materials, 63, 2014, 97-107. https://doi.org/10.1016/j.conbuildmat 2014.03.045.
10. J. Liu et al.: Ceramics International, 44, 2018, https://doi.org/10.1016/j.ceramint.2018.04.151.
11. H. Lee, A. Hanif, M. Usman, J. Sim, H. Oh: Journal of Cleaner Production, 170, 2018, https://doi.org/10.1016/j.jclepro.2017.09.133.
12. N. Tangboriboon, W. Pannangpetch, A. Khomkrit, K. Petcharoen, A. Sirivat: Progress in Rubber Plastics Recycling Technology, 31, 2015, 189-206. https://doi.org/10.1177/147776061503100304.
13. H. Abdeen, S. Shihada: Journal of Scientific Research and Reports, 13, (2017), 1-9, https://doi.org/10.9734/JSRR/2017/32174.
14. I. Demir: Journal of the International Solid Wastes and Public Cleansing Association, ISWA. 27, 2009, 572-577. https://doi.org/10.1177/0734242X08096528.
15. S. Hariharan, G. Jebaraj: International Journal of Research in Computer Applications and Robotics, 6(2), 2018, 1-24. Available at https://ijrcar.com/Volume_6_Issue_2/v6i201.pdf.
16. ASTM D6913-17: *Standard Test Methods for Particle Size Distribution (Gradation) of Soils Using Sieve Analysis*. ASTM International. West Conshohocken, PA. 2017.
17. ASTM C 1314-18: *Standard Test Methods for Compressive Strength of Masonry Prisms*, ASTM International. West Conshohocken, PA. 2018.
18. ASTM 293/C293M.: *Standard Test Methods for Compressive Strength for Flexural Strength of Concrete (Using Simple Beam with Centre-Point Loading)*, ASTM International. West Conshohocken, PA, 2016.

19. IS 2720 Part 3: *Method of Test for soil. Bureau of Indian Standards.* Manak bhavan, 9 Bahadur Shah Zafar Marg, New Delhi. 1980.
20. BS 1377-2: *Methods of Test for Soils for Civil Engineering Purpose. Chemical and Electrochemical Testing*. British Standard Group. United Kingdom. 1990.
21. IS 383-1970: *Specification for Coarse and Fine Aggregates from Natural Sources for Concrete*. Bureau of Indian Standards. Manak bhavan, 9 Bahadur Shah Zafar Marg, New Delhi, 1970.
22. ASTM C136/C136M.– 19: *Standard Test Methods for Sieve Analysis of Fine and Coarse Aggregates*, ASTM International. West Conshohocken, PA. 2019.
23. Z.U. Elakhame, F. Ifebhor, W.A. Asotah: Journal of Science, Engineering and Technology, Kathmandu University, 12(2), 2016, 50-59.
24. Australian Standard for Masonry Structures AS3700 (2001). *Engineering Design of Earth Buildings.* Sydney. NSW, 2001.
25. ASTM D790-10: *Standard Test Methods for Compressive Strength for Flexural Strength of Concrete (Using Simple Beam with Centre-Point Loading)*, ASTM International. West Conshohocken, PA. 2010.

ACTA METALLURGICA SLOVACA
2021, VOL. 27, NO. 1, 11-16

RESEARCH PAPER

EFFECT OF DIFFERENT STRAIN ROUTES ON MECHANICAL PROPERTIES AND MICROSTRUCTURE OF COPPER

Seyed Mohammad Javad Hoseini[1], Hamid Ghayour[1*], Ali Salemi Golezani[2], Masoud Kasiri Asgarani[1], Iman Ebrahimzadeh[1]

[1] Advanced Materials Research Center, Department of Materials Engineering, Najafabad Branch, Islamic Azad University, Najafabad, Iran.
[2] Department of Materials Engineering, Karaj Branch, Islamic Azad University, Karaj, Iran.

*Corresponding Author's email: ghayour_ham@iust.ac.ir, Tell: +98 9132308300, Department of Materials Engineering, Najafabad Branch, Islamic Azad University, Najafabad, Iran.

Received: 10.08.2020
Accepted: 24.09.2020

ABSTRACT

In the current paper, the role of change in strain routes was investigated, along with the cold rolling of copper metal. Four different strain routes including, (a) unidirectional rolling, (b) reverse rolling, (C) two-stage cross-rolling, and (d) multi-stage cross-rolling, were utilized to investigate the effect of strain routes change on microstructure, texture evolution, and anisotropy. Tensile strength in the unidirectional rolling sample compared to the cross-rolling sample decreased in the direction of initial rolling from 364 MPa to 340 MPa, in the direction of 45˚ to the initial rolling from 359 MPa to 347 MPa, and in the direction of perpendicular to the initial rolling from 371 MPa to 360 MPa. Texture intensity also decreased from 1413 in the unidirectional rolling sample to 992 in the cross-rolled sample. The results demonstrated that by rolling in different routes, the cross-rolling has led to a more homogeneous microstructure, less anisotropy, and weaker texture.

Keywords: Reverse Rolling; Cross Rolling; Unidirectional Rolling; Copper; Change strain Route

INTRODUCTION

Change in strain routes during the deformation process affects metal plastic behaviors, such as the crystallographic texture evolution [1]. The main focus of strain route change is on the production of metal sheets with different textures and microstructures, indicating different properties [2]. The change in the strain route can be achieved by changing the rolling direction (RD) alternately. For instance, in the rolling process, four types of changes are considered for the strain route, being classified into (1) Unidirectional Rolling (UR), (2) Reverse Rolling (RR), (3) Two-Stage Cross-Rolling (TSCR), and (4) Multi-stage cross-rolling (MSCR) (Fig.1) [3,4].

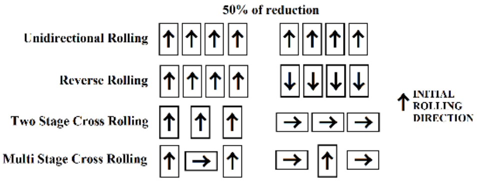

Fig. 1 Schematic of different rolling modes to show the change in strain route [5, 6]

The strain route changes have a significant impact on the evolution of microstructure and texture during the rolling of metals, especially fcc metals, such as copper. Strain route changes in the rolling process due to the weaker texture created by the rolling can provide more homogeneous properties. Therefore, such changes can be a unique way to improve material properties [5]. In this regard, the effects on the materials as a result of changes in the direction of deformation are as follows: Changes in microstructure and crystallographic texture, Changes in plastic anisotropy, Changes in residual stress distribution [7, 9].

One of the solutions that may be suggested by changes in the strain route is to tailor the texture to control the formation of the desired texture components and eliminate undesired texture components [1, 8]. Additionally, Zhang et al. [10], concluded that changing the strain route could lead to an increase in the strength and ductility, grain refinement, and weaker texture. Goli et al. [11] also concluded that in the cross-rolled sheet sample, the grain size was smaller than in the unidirectional-rolled sheet and the reverse-rolled sheet; moreover, the effect of dynamic recrystallization could be observed. The local serrations of grain boundaries and the nucleation at pre-existing boundaries indicate the occurrence of discontinuous dynamic recrystallization (DDRX) mechanism. It should be noted that the number of dynamically recrystallized grains in cross-rolled samples is higher in comparison to unidirectional-rolled and reverse-rolled samples, which is leading to smaller grain size in cross-rolling specimens. In unidirectional-rolling specimens, the number of active sliding systems is less than in those of cross-rolling that is leading to a severe dislocation pile-up. In other words, cross rolling leads to the activation of numerous slip systems; consequently, it results in increasing cross slip possibility and recovery and recrystallization rates. Yang et al. [12] reported that in Al-Mg-Si alloys, a right combination of strength and flexibility was obtained by performing reverse rolling.

Cold working (e.g., rolling) on metals leads to orienting the microstructure along with the deformation. The orientation of the microstructure causes the orientation of mechanical properties; ultimately, it results in anisotropy occurrence. The value of R, called the plastic anisotropy. The average amount of anisotropy in different directions, or R_m, which is also called vertical anisotropy, is equal to one ($R_m = 1$) for a perfectly isotropic material and indicates the strain and strength equality in the thickness and width directions of the sheet. The value of Rm depends on several factors, such as the chemical composition of the alloy, Young's modulus, primary grain size, amount of strain, and its angle to the rolling direction [13]. Plastic anisotropy (R) indicates the resistance of the sheet against any changes in the thickness. In other words, the ratio of true strain in the width direction (ε_w) to true strain in the thickness direction (ε_t) in the uniaxial tension test is called the plastic anisotropy [14].

$$R = \frac{\varepsilon_w}{\varepsilon_t} \quad (1.)$$

where: R- plastic anisotropy
ε_w- true strain in the width direction
ε_t- true strain in the thickness direction

Generally, the value of R is not equal to one. It reveals the difference of the behavior in the two directions of the sheet (width and thickness)[14]. The average value of R_m is defined as below:

$$R_m = \frac{R_{0^\circ} + 2R_{45^\circ} + R_{90^\circ}}{4} \quad (2.)$$

where: R_m- average of anisotropy in different directions
R_{0°- strain ratio in the longitudinal direction
R_{45°- strain ratio measured 45° to the rolling direction
R_{90°- strain ratio in the transverse direction.

Samples are prepared at 0°, 45°, and 90° directions concerning the rolling direction of the sheet [12]. R_m is weighted average of r values obtained in three directions: 0° (parallel), 45° (diagonal), and 90° (transverse) to the rolling direction. Planar anisotropy (eq.(3)) is another significant indicator that one of the applications of which is the expression of the degree of earring of the edges that occur on the sides of the deep drawing specimens [15,16]. For a perfectly isotropic sheet, the following equations of $\Delta R=0$ and $R_m=1$ must apply. In some cases, the orientation of the mechanical properties is undesirable and must be controlled [13]. One of the ways to reduce the value of R_m and control the anisotropy phenomena is recrystallization and annealing heat treatment [17, 18].

$$\Delta R = \frac{R_{0^\circ} - 2R_{45^\circ} + R_{90^\circ}}{2} \quad (3.)$$

where: ΔR- planar anisotropy
R_{0°- strain ratio in the longitudinal direction
R_{45°- strain ratio measured 45° to the rolling direction
R_{90°- strain ratio in the transverse direction.

Many researchers have investigated the effect of strain routes in the cold rolling process on microstructure, mechanical properties, anisotropy, and texture of various alloys. However, the effect of different strain routes in the C11000 copper alloy on the same four features has not been studied altogether. Therefore, in the present study, the effect of various strain routes in cold rolling (including unidirectional rolling, cross rolling, and reverse rolling) on the mentioned four features of copper alloy C11000 is investigated.

MATERIAL AND METHODS

All samples were subjected to a complete annealing process at 600 ˚C and 1 hour respectively temperatures and times. Samples were subjected to the rolling process according to the routes provided in Table 2. These routes are displayed schematically in Fig. 2. A rolling machine performed cold rolling with two rollers that have a diameter of 350 mm. The rolling speed was 10 meters per minute. The final thickness of the rolled sheets was 2.5 mm. Finally, a total 50% reduction in thickness was observed in sheets.

Table 1 Chemical analysis of C11000 alloy

Element	%wt
Cu	99.9869
O	0.013
P	0.0039
S	0.0008
Al	0.0004
Pb	0.0015
Ni	0.0012
Zn	0.0011
Sb	0.0009
Si	0.0002

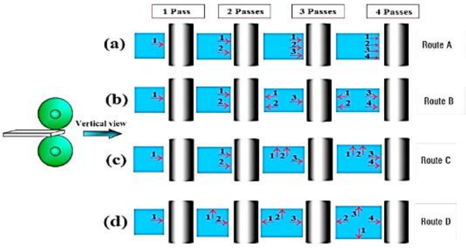

Fig. 2 Schematic of different rolling routes

The rolled specimens in three different planes (are shown in Fig.3), were cut and mounted, and the polishing process was performed and were etched in a solution (150 cc Hcl + 10gr$Fecl_3$ + 100cc H_2o) and examined under an optical microscope. Tensile test samples were prepared according to ASTM E8M standard from different cycles of rolled parts to investigate the difference between mechanical and anisotropy properties in three directions of 0, 45, and 90 degrees with respect to the initial rolling direction according to ASTM E517 and ISO 10113 (are shown in Fig.4). Texture measurements were carried out by a Philips X'pert MPD X-ray texture diffractometer that is utilizing Cu Kα radiation.

Table 2 Schedule for different routes of the rolling process (final thickness as 2.5 mm)

Samples	Deformation steps
A	Unidirectional Rolling (UR) reduction: 50% in RD
B	Reverse Rolling (RR) reduction:25% in RD and 25% in RR
C	Two Stage Cross Rolling (TSCR) reduction:25% in RD and 25% in CR
D	Multi Stage Cross Rolling (MSCR) reduction:12.5% in RD + 12.5% in CR+ 12.5% RR+ 12.5 % CR

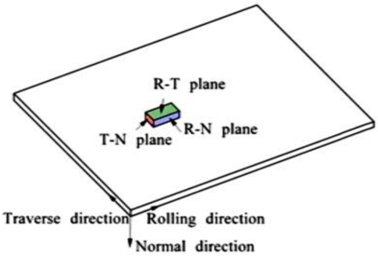

Fig. 3 Illustrations of sampling location in rolling samples

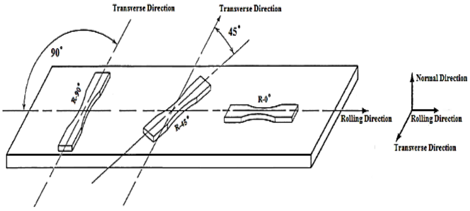

Fig. 4 Preparation of tensile test samples in three directions of 0°, 45°, and 90°

RESULTS AND DISCUSSION

Microstructure

The microstructure images of three sections of these specimens are illustrated in Fig.5, Fig.6, Fig.7, and Fig.8.

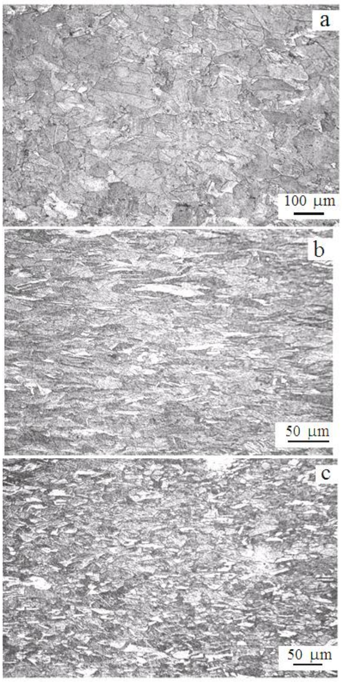

Fig. 5 Optical micrographs related to A sample and in sections (a) of the R-T plane, (b) the R-N plane, and (c) the T-N plane

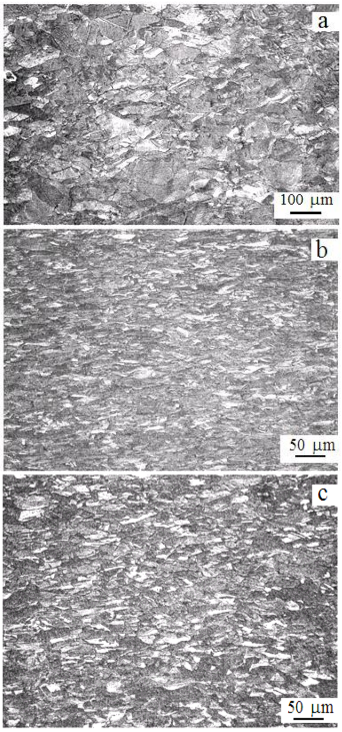

Fig. 6 Optical micrographs related to B sample and in sections (a) of the R-T plane, (b) the R-N plane, and (c) the T-N plane.

In rolled specimens in different routes, the grains were elongated according to the amount of strain and its direction in the last rolling pass, and bands were formed with different widths. In the B sample, which reversed the rolling direction, the grain size got decreased in comparison to the A sample. Additionally, the average length of the grains decreased; however, the width of the grains showed little variations (Table 3). By increasing cross rolling, the grain size decreased. In cross-rolled specimens (C and D), the aspect ratio was slightly different on the two planes of TN and RN. Samples with higher cross rolling had a more homogeneous microstructure. Furthermore, twinning was observed in all samples of rolled copper. In cross-rolling and reverse-rolling specimens, the mentioned twinnings are more common in general.

Dislocation slip is known as the primary ruling mechanism during plastic deformation, which leads to the formation of dislocation cells, dislocation walls, or micro bands, depending on the imposed strain and initial orientation. Moreover, shear bands occur as a specific manifestation of local plastic instability at medium to large strains [19, 20]. In the microstructure images of rolled samples, shear bands are visible. Sawas et al. [6] also observed shear bands in microstructure images of rolled copper specimens. They indicated that by performing two-step cross rolling, the direction of shear bands changed in comparison to the unidirectional rolling sample, and in multi-step cross rolling, shear bands were present in both directions. The mentioned shear bands that have been formed in two different directions during unidirectional and cross rolling are also observed in other researchers' studies, including Pospiech [21].

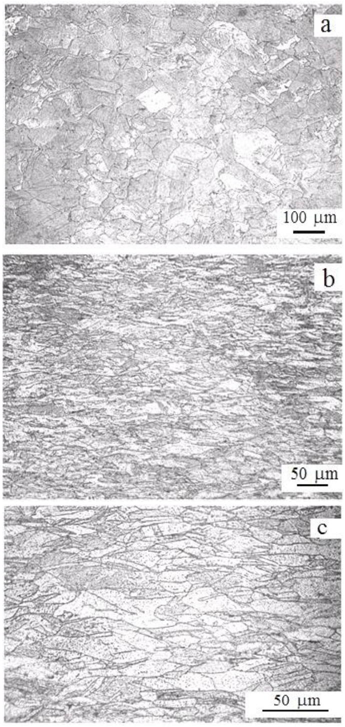

Fig. 7 Optical micrographs related to C sample and in sections (a) of the R-T plane, (b) the R-N plane, and (c) the T-N plane

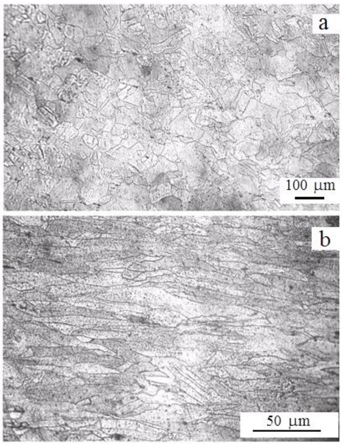

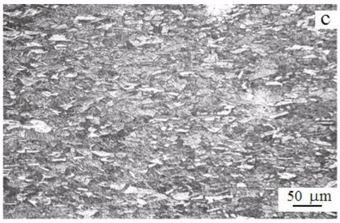

Fig. 8 Optical micrographs related to D sample and in sections (a) of the R-T plane, (b) the R-N plane, and (c) the T-N plane.

Table 3 Average grain size and aspect ratio in R-T, R-N, and T-N planes in rolling samples

sample name	R-N plane		T-N plane		R-T plane	
	aspect ratio	average grain length (μm)	aspect ratio	average grain length (μm)	aspect ratio	average grain length (μm)
A	3.97	23.08	6.65	40.33	2.44	35.47
B	3.69	21.80	5.41	33.25	2.50	33.72
C	4.09	25.47	5.72	31.28	2.17	33.02
D	5.04	27.15	5.90	29.74	2.65	31.01

Tensile test

The diagrams obtained from the tensile test in three directions of 0, 45, and 90 degrees relative to the first rolling direction (RD) are illustrated in Fig.9; moreover, the comparison diagrams of strength and elongation in different rolling routes are shown in Fig.10 (a) and (b), respectively. As can be observed, cold rolling operations on different routes resulted in increased strength and reduced elongation in all three directions of tensile test 0, 45, and 90 degrees. The mentioned fact was due to an increase in work hardening, an increase in the density of dislocation, and a decrease in grain size. Additionally, the highest strength in these samples occurred in A and B. The strength in the two directions of 0 and 45 degrees in the B sample regarding the reverse rolling was more than the A sample regarding the unidirectional rolling. Moreover, the elongation increased in all the three directions in the B sample (reverse rolling) in comparison to A sample. In general, the use of the reverse-rolling process in copper alloy C11000 increased the strength and elongation to the failure property in comparison to unidirectional rolling samples; furthermore, it improved the mechanical properties of reverse rolling compared to the unidirectional one. The reason for this can be attributed to grain refinement, dislocations interaction, and lower aspect ratio (relation between the length and width of the grain) in the reverse-rolling specimen in comparison to unidirectional one. Sabat et al. [22] obtained similar results for unidirectional and reverse rolling in titanium alloys. They confirmed the increase in dislocation density and energy stored in reverse rolling to unidirectional rolling.

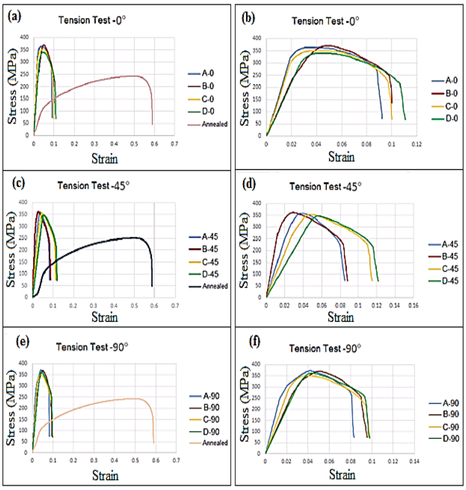

Fig. 9 Diagram of the tensile test in the direction of (a) and (b) 0˚, (c) and (d) 45˚, (e) and (f) 90˚ with respect to the direction of first rolling in the rolled samples.

It can also be attributed to grain refinement, grain size reduction, and lower aspect ratio in the reverse rolling sample compared to that of unidirectional rolling, as well. In the C and D samples, in which different cross rolling occurred, the tensile and yield strengths were less than the unidirectional rolling (sample A) and reverse rolling (sample B).

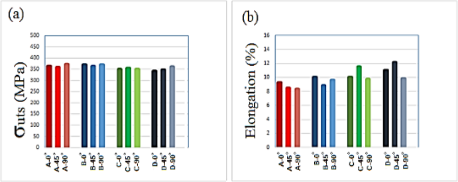

Fig. 10 Comparison (a) of tensile strength and (b) elongation in rolled specimens in different routes

Moreover, the elongation to failure property of these samples increased compared to A and B samples. According to the research of Ostafin et al. [8], the change in the direction of plastic strain on copper sheets caused significant changes in the distribution of grain orientation (crystal texture) and the microstructure of the material; these changes led to changes in plastic behavior and mechanical properties, such as strength and softness of the deformation. They found that changing the strain route and cross rolling of copper sheets resulted in forming a combination of desirable textures, reducing undesirable textures, and creating more uniform properties.

Reduction in grain size could lead to an increase in strength in cross-rolling specimens, whereas cross rolling reduced strength and increased the elongation relative to unidirectional rolling. The stated fact may be due to weaker crystalline texture and dynamic recrystallization due to the strain route change. The achieved results were also observed in the research of Zhang Hua [10] et al. and Rout [7] et al.

Anisotropy

The values of R_m anisotropy in the rolled samples were calculated according to the strain obtained in the longitudinal and transverse directions of the tensile test samples.

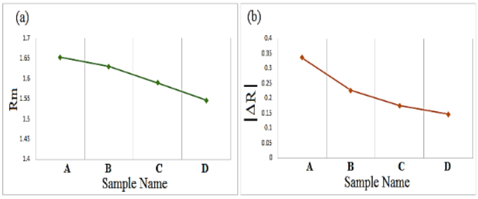

Fig. 11 Comparison diagrams between values of (a) planar anisotropy in rolled specimens, (b) anisotropy of rolled specimens

According to the obtained values of ΔR and R_m for rolling samples in different routes, the diagrams in Fig.11, it can be concluded that the values | ΔR | and Rm decreased by changing the strain direction and also occurring cross rolling. Thus, similar to the results obtained by Goli et al. [11], changing the strain direction and cross rolling has been an effective method to reduce the anisotropic mechanical properties of C11000 copper alloy sheet. These results are in line with those of other researchers, including Wronski et al. [9] and Rout et al. [7]. Therefore, changing the strain direction in the C11000 copper alloy sheet can lead to the production of a sheet with relative isotropic properties in different directions in comparison to unidirectional rolling.

Microhardness test

The Vickers microhardness test was performed on rolled specimens on three planes of RT, TN, and RN and compared in Fig.12. In this regard, the amounts of microhardness on the TN plane is higher than the other two planes. Additionally, in all samples, the values of microhardness on the RT plane is less than the other two planes. The microhardness values obtained in this experiment are in good agreement with the microstructure and grain size obtained from the metallography of the rolled samples.

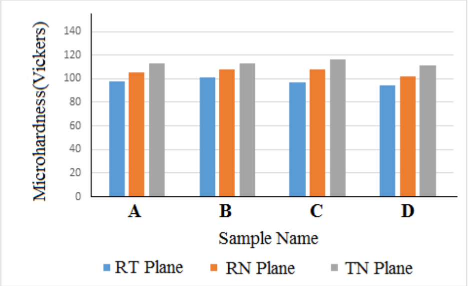

Fig. 12 Comparison diagrams of the values for microhard-ness in different routes and planes

Crystallographic texture

Changing the deformation route has a major effect on the formation of cold rolling texture. The (1 1 1) pole figures for the deformed specimens in four different routes are presented in Fig.13. As observed, the texture present in A and B samples represents the texture of FCC metals, with the medium and high stacking fault energy. Texture in copper is characterized by compounds, including Cu {112}(111), Bs {110}(112), and S {123}(634) [5]. The texture of D and C specimens are significantly different from the corresponding texture of A and B specimens for copper. The texture of cross-rolling specimens (C and D) is relatively weaker than that of unidirectional-rolling and reverse-rolling specimens. As demonstrated in Fig.13, which is presented the pole figure of the rolling specimens in different routes, the unidirectional-rolling specimen has the highest intensity; additionally, the texture intensity in the reverse rolling is less than the unidirectional rolling and more than the cross rolling. The multi-stage cross-rolling specimen has the lowest texture intensity. These results are similar to results of other researchers [23, 24].

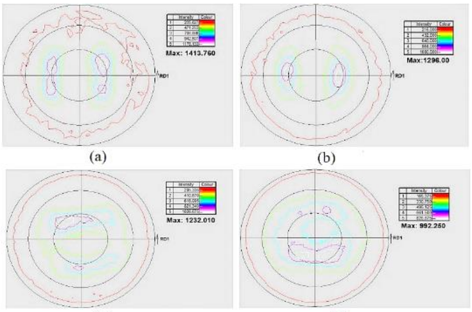

(a) (b)
(c) (d)

Fig. 13 Pole figures (111) of (a) A, (b) B, (c) C, and (d) D samples

CONCLUSION

Changes in mechanical properties, anisotropy, microstructure, and texture of C11000 copper after unidirectional, reverse rolling, and cross rolling are investigated in the present study. The microstructure of the rolled samples includes the stretched grains along the last rolling direction, which is indicating the deformation band and reduced grain size. Changing the routes of plastic strain on the copper sheet causes significant changes in the material's microstructure. Cross rolling in C and D samples reduces grain size compared to unidirectional and reverse rolling. Grains are also stretched along with the last steps of the rolling. Changing the strain routes and performing cross rolling in copper metal reduce the strength compared to unidirectional and reverse rolling samples (from 371 Mpa to 340 Mpa) and increase the ductility to some extent (from 8.5 to 12). Plastic anisotropy in cross-rolling samples is less than unidirectional and reverse rolling specimens. X-Ray results reveal that texture intensity in rolling specimens in different routes is not equal. The texture intensity in cross-rolling specimens (992) is lower than in unidirectional-rolling (1413) and reverse-rolling (1296) specimens. One of the reasons for the lower anisotropy of cross-rolling specimens in comparison to those of unidirectional and reverse rolling can be the more moderate texture intensity in these specimens.

REFERENCES

1. S. Suwas, A.K. Singh: Materials Science and Engineering A, 356(1-2), 2003, 368-371.
https://doi.org/10.1016/S0921-5093(03)00149-7.
2. W. Chen,Y. Lv, H. Wang, X. Zhang, C. Chen, Y.C. Lin, K. Zhoua: Materials Science and Engineering: A, 769, 2020, 138516.
https://doi.org/10.1016/j.msea.2019.138516.
3. M. Benke, B. Schweitzer, A. Hlavacs, V. Mertinger: *Metals*, 10(2), 2020, 192. https://doi.org/10.3390/met10020192.
4. S. Suwas, N. Gurao: Comprehensive Materials Processing, 3, 2014, 81-106.
https://doi.org/10.1016/B978-0-08-096532-1.00308-3.
5. N. Gurao, S. Sethuraman, S. Suwas: Materials Science and Engineering A, 528(25-26), 2011, 7730-7750.
https://doi.org/10.1016/j.msea.2011.06.062.
6. S. Suwas, A. K. Singh, K. Narasimha Rao, T. Singh: Carl Hanser Verlag, Munchen Z. Metallkd, 93(9), 2002, 918-927.
https://doi.org/10.3139/146.020918.
7. M. Rout, S. K. Pal, S. B. Singh: Cross Rolling: A Metal Forming Process, In: Modern Manufacturing Engineering, Materials Forming, Machining and Tribology, Springer International Publishing Switzerland, 2015, 41-66.
https://doi.org/10.1007/978-3-319-20152-8_2.
8. M. Ostafin, J. Pospiech, R.A. Schwarzer: Solid State Phenomena, 105, 2005, 309-314.
https://doi.org/10.4028/www.scientific.net/SSP.105.309.
9. S. Wronski, M. Wrobel, A. Baczmanski, K. Wierzbanowski: Materials Characterization, 77, 2013, 116-126.
https://doi.org/10.1016/j.matchar.2013.01.005.
10. H. Zhang, G. Huang, H. J. Roven, L. Wang, F. Pan: Materials and Design, 50, 2013, 667-673.
https://doi.org/10.1016/j.matdes.2013.03.053.
11. F. Goli, R. Jamaati: Materials Research Express, 6(6), 2019.
https://doi.org/10.1088/2053-1591/ab0a1f.
12. H. Yang, I. Widiantara, Y. Ko: Materials Letters, 213, 2018, 54-57.
https://doi.org/10.1016/j.matlet.2017.11.012.
13. W. F. Hosford and R. M. Caddell: *Metal Forming Mechanics And Metallurgy*, Third Edition, Cambridge University Press, 2007.
14. Dieter G.E.: *Workability Testing Techniques. ASM Handbook*. Vol. 8, 1999.
15. ASTM E517: Standard Test Method for Plastic Strain Ratio r for Sheet Metal, *ASTM International*, Conshohocken, 2000.
16. ISO 10113: Metallic Materials- Sheet and strip- Determination of plastic strain ratio, *International Standard*, Switzerland, 2006.
17. X. Chen, L. Wang, R. Xiao, X. Zhong, G. Huang, Q. Liu: Journal of Alloys and Compounds, 604, 2014, 112-116.
https://doi.org/10.1016/j.jallcom.2014.03.093.
18. Y. Ma et al.: Progress in Natural Science: Materials International, 28(6), 2018, 711-717.
https://doi.org/10.1016/j.pnsc.2018.10.004.
19. Y. Xu, H. Jiao, W. Qiu, R. D. K. Misra, J. Li: Materials,11(7), 2018,1161. https://doi.org/10.3390/ma11071161.
20. A. Sonboli, M. R. Toroghinejad, H. Edris and J. A. Szpunar: International Journal of Iron & Steel Society of Iran, 12(2), 2015, 1-6.
21. J. Pospiech: Archives of Metallurgy and Materials, 53(1), 2008, 83-87.
22. R. K. Sabat, S. K. Sahoo, B. D. Bishoyi, N. Bibhanshu, S. Suwas: Philosophical Magazine Letters, 97(7), 2017, 273-279.
https://doi.org/10.1080/09500839.2017.1341647.
23. D. K. Liu, G. S. Huang, G. L. Gong, G. G. Wang, F. S. Pan: Transactions of Nonferrous Metals Society of China, 27(6), 2017, 1306-1312.
https://doi.org/10.1016/S1003-6326(17)60151-1.
24. Y. Chino, K. Sassa, A. Kamia, M. Mabuchi: Materials Transactions, 47(10), 2006, 2555-2560.
https://doi.org/ 10.2320/matertrans.47.2555.

ACTA METALLURGICA SLOVACA
2021, VOL. 27, NO. 1, 17-22

RESEARCH PAPER

HYDROMETALLURGICAL NICKEL AND COBALT PRODUCTION FROM LATERITIC ORES: OPTIMIZATION AND COMPARISON OF ATMOSPHERIC PRESSURE LEACHING AND PUG-ROAST-LEACHING PROCESSES

Ozan Coban[1,4], Serkan Baslayici[2,4]*, Mehmet Bugdayci[2,3], Mahmut Ercan Acma[4]

[1] Metallurgical and Materials Eng. Department, Istanbul Gedik University, 34876, Istanbul, Turkey
[2] Construction Technology Department, Istanbul Medipol University Vocational School, 34810, Istanbul, Turkey
[3] Chemical Engineering Dept. Yalova University, 77200 Yalova, Turkey
[4] Metallurgical and Materials Eng. Dept., Istanbul Technical University, 34469, Istanbul, Turkey

*Corresponding Author's email: sbaslayici@medipol.edu.tr, Construction Technology Department, Medipol University Vocational School, 34810, Istanbul, Turkey

Received: 01.11.2020
Accepted: 01.01.2021

ABSTRACT

Corresponding to the technological developments, production and consumption of nickel have increased greatly over time due to its unique mechanical and chemical properties. Therefore, the production of nickel will always keep its importance. The availability of laterite ores, which are oxide type ores, is 86% of the nickel reserves on the Earth, and the processes used in the production of nickel from sulphide type ores have negative environmental effects. Therefore, recovery of nickel from lateritic ores has become increasingly important in recent years. In this study, the aim was to determine the optimum parameters of nickel and cobalt production from limonite type lateritic nickel ores, which were taken from Manisa Caldag region of Turkey, using atmospheric pressure sulfuric acid leaching and pug-roast-leach process. When the results obtained in these processes were compared, it was found that the Ni leaching efficiency is nearly 8% higher and iron leaching efficiency (contamination) is nearly 4% lower in the pug-roast-leach process. Furthermore, the pug-roast-leach process was completed in 33% lower time compared to the atmospheric pressure sulfuric acid leaching process.

Keywords: Nickel; Cobalt; Hydrometallurgy; Pug-Roast-Leaching; Atmospheric Pressure

INTRODUCTION

Mainly, there are two types of nickel-containing ore deposits. These are sulfide type and laterite types. The sulfide type may contain up to 4% nickel, but on average, it contains from 1% to 2% nickel by weight. Sulfide type minerals' availability is about 14% of the total known nickel reserves. Lateritic oxide ores are considered as the main resources of nickel. Recovery of nickel from laterite ores is becoming increasingly important since their availability is 86% of the nickel reserves on the Earth [1-7].

Extraction of nickel from ores with high Ni/Fe ratio and low moisture content is carried out by pyrometallurgical processes. These processes are also used in nickel extraction from ores with high magnesium content. Disadvantages of pyrometallurgical processes such as high-grade ore requirement, metal loss with slag, high energy requirement, SO_2 removal problems and low cobalt recovery rate increase the cost of nickel production [8]–[16]. Also, high amount of hydrocarbon fuels, coal, oil, naphtha and electricity are used in pyrometallurgical processes. It is necessary to consider the percentages of iron, magnesium and silica which control viscosity, electrical conductivity and melting point of the slag. For all the above reasons, hydrometallurgical processes are preferred instead of pyrometallurgical processes [17-20].

In recent years, there have been studies on the recovery of nickel and cobalt from lateritic ores.

The formation of lateritic rocks on the surface of the Earth occurs over a long time period and is effected by temperature changes and rainfall. Laterite formation begins with the chemical and mechanical effects of air, water and heat, as well as the decomposition of minerals containing magnesium, iron, nickel, cobalt and other components to the generate solution. These solutions percolate to the lower zones over time and finally, lateritic nickel ores which are economically feasible for the recovery of nickel are formed. Lateritic nickel ore deposits with 1% to 3% grade are formed by the decomposition of ultramafic rocks, which contain nickel and cobalt between 0.1% to 0.3%. The decomposition of ultramafic rocks occurs due to atmospheric and hydrospheric phenomena [21–28].

Extraction of nickel from nontronitic or limonitic laterites which have a low Ni/Fe ratio is possible through hydrometallurgical processes. In these processes, leaching of nickel by mineral and/or organic acids can be utilized. Hydrometallurgical processes that are applied to lateritic ores can be divided into three groups such as high-pressure acid leaching, atmospheric pressure acid leaching and acid pug-roast-leach process. High-pressure acid leaching has advantages like; obtaining high metal recoveries (95% for Ni and Co) from limonitic laterites; and eliminating high energy and time-consuming steps such as drying, calcination and reduction. However, high

DOI: 10.36547/ams.27.1.740

investment costs due to autoclave lining (titanium lining or acidic brick and lead lining), flash tanks and other expensive equipment are disadvantages of high-pressure acid leaching. Atmospheric pressure acid leaching has advantages such as both providing to utilize saprolitic ores with magnesium content over 6% and also no need for high-cost autoclaves and also high metal recovery. On the other hand, iron is passing to the solution with nickel and cobalt in this process. Contaminants such as Fe, Al, Cr, Mn and Mg, other than nickel and cobalt, are removed by precipitation of these elements and/or separation of nickel and cobalt from the solution to produce nickel and cobalt. Pug-roast-leaching processing can be used as an alternative method for the dissolution of lateritic ore at atmospheric pressure by using sulfuric acid [29–36]. This can be considered as an improved version of the atmospheric pressure sulfuric acid leaching due to the fact that water insoluble oxides are converted to water soluble sulphates. Considering all the above factors, it was decided to use pug-roast-leaching process in the experimental studies in order to see how these processes could be improved and how the disadvantageous sides could be eliminated of atmospheric pressure acid leaching process [27–36].

The aim of this study is to determine the optimum parameters for nickel and cobalt production from limonite type lateritic nickel ores, which were taken from Manisa Caldag region of Turkey, through atmospheric pressure sulfuric acid leaching and pug-roast-leaching processes. An additional aim was to investigate the parameters and the kinetics of the hydroxide precipitation which is carried out after the leaching process.

MATERIAL AND METHODS

In this study, production of nickel and cobalt from limonite type lateritic nickel ores by using hydrometallurgical processes was investigated. In experimental studies, atmospheric pressure sulfuric acid leaching and pug-roast-leaching processes were used to leach nickel from the ore to solution. These processes were applied to milled lateritic nickel ores and leaching efficiencies were compared. Iron removal and mixed hydroxide precipitation processes were applied to pregnant solutions after extraction of the nickel.

Limonite based lateritic nickel ores, which were taken from Manisa Caldag region of Turkey, were used in the experimental studies. Samples of 10 grams of ore were used in each experiment. Chemical analysis of lateritic ore used in the experiments is given in Table 1. The mean grain size of the ore, for which the particle size distribution is shown in Figure 1, was determined to be 27.76 µm. Particle size measurement was carried out with Malvern Mastersizer 2000. Perkin Elmer Aanalyst 800 AAS (Atomic Absorption Spectrometry) was used in chemical analyses for solutions.

Table 1 AAS results of lateritic ore (wt, %)

Ni	**Fe**	**Co**	**Cu**
1.41	24.94	0.062	0.001
Zn	**Al_2O_3**	**CaO**	**Cr_2O_3**
0.026	4.00	0.66	1.13
K_2O	**MgO**	**MnO**	**Na_2O**
0.25	5.88	0.38	0.08
P_2O_5	**Pb**	**TiO_2**	**SiO_2**
0.03	<0.005	0.13	40.90

Drying of the ore before atmospheric pressure acid leaching and pug-roast-leaching processes was carried out in Thermo Scientific Heraeus drying oven. Leaching experiments were conducted using a magnetic stirrer.

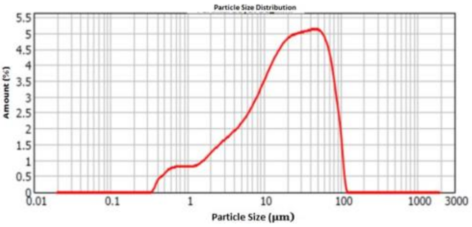

Fig. 1 Particle size distribution of the lateritic ore

The ore was ground in a vibratory cup mill. In the experimental studies, two methods were used to extract the nickel and cobalt from ore. These are atmospheric pressure sulfuric acid leaching and pug-roast-leaching processes. The flowchart for the experimental studies is given in Figure 2.

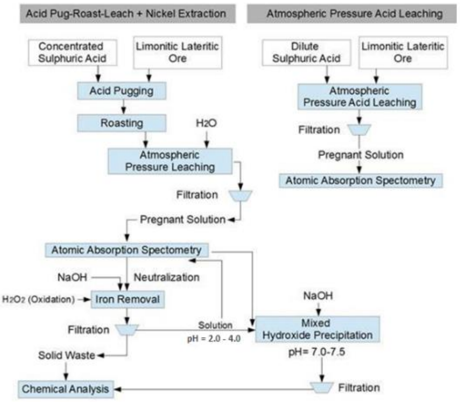

Fig. 2 Flowchart of the experimental studies

Samples of 10 grams of lateritic ore (per experiment), dilute sulfuric acid (H_2SO_4), magnetic stirrer (800 rpm) and filtration system were used in atmospheric pressure acid leaching experiments. Effects of leaching time, acid concentration, leaching temperature, particle size and pulp density on nickel, cobalt and iron leaching efficiencies were investigated. Initially, leaching time experiments were executed. Samples were leached for 30, 60, 90, 120, 150 minutes and the optimum leaching time was determined. Acid concentration experiments were carried out after the optimum leaching time was determined. Samples were leached with sulfuric acid having concentrations of 50, 100, 150, 200 g/l and optimum concentration was determined. Then, the effect of leaching temperature was investigated. Samples were leached at 40, 50, 60, 70, 80, 90°C and the optimum leaching temperature was determined. Particle size experiments were carried out after optimum leaching time, acid concentration and leaching temperature were determined. These optimum parameters were used in the leaching of particles with different average particle sizes. These sizes were 38, 74, 100, 150 and 300 micrometers. Finally, pulp density experiments were carried out by using leaching solutions for 10, 20, 30 and 40% pulp densities in order to determine the optimum pulp density value for atmospheric pressure leaching process.

Samples of 10 grams of lateritic ore, concentrated sulfuric acid (96-98% purity), atmosphere-controlled furnace, magnetic stirrer (800 rpm), distilled water and filtration system were used in acid pug-roast-water leaching experiments. The effects of acid/ore ratio, roasting time, roasting temperature, leaching duration and pulp density on nickel, cobalt and iron leaching efficiencies were investigated. Theoretical sulfuric acid quantity needed for roasting was calculated as 7 grams of H_2SO_4 per 10 grams of ore according to the chemical analysis of the ore. Acid/ore ratio experiments were carried out with 0.7, 1.0, 1.5, 2.0 grams of acid per 1 gram of ore. After the optimum amount of acid addition was determined, roasting time experiments were executed. Samples were roasted for 30, 60, 90, 120, 150 minutes and the optimum roasting time was determined. Then, the effect of roasting temperature was investigated by roasting the samples at 100, 150, 200, 250 and 300 °C. After the roasting operation, the optimum leaching time was investigated. Samples, which were roasted at optimum conditions, were leached for 30, 60, 90, 120 and 150 minutes by using distilled water. In pulp density experiments, distilled water was used as the solvent and it was added according to the amount of ore used. Pulp densities used in this experiment were 0.10, 0.125, 0.17, 0.25 and 0.50g/ml.

After leaching was performed at optimum conditions in pug-roast-leaching process, iron removal and mixed hydroxide precipitation experiments were performed. For iron removal, oxidation of Fe^{+2} to Fe^{+3} was undertaken using 40 ml of 35% H_2O_2 added to 200 ml of leaching solution with a pH of 1 and stirred with a magnetic stirrer for 15 minutes. Then, the pH of the solution was increased by adding NaOH. The amount of NaOH was calculated stoichiometrically according to Equation 1. It was found that pH value was increased to 4.0 with approximately 40 ml NaOH addition and iron was precipitated as $Fe(OH)_3$. Iron removal efficiencies according to the changing pH values were also investigated.

$$Fe_2(SO_4)_3 + 6NaOH \rightarrow 3Na_2SO_4 + 2Fe(OH)_3 \quad (1.)$$

After iron removal was completed, mixed hydroxide precipitation was conducted. The stoichiometric NaOH amount was calculated as 0.15 grams according to Equation 2 and Equation 3. The pH of the solution was increased from 4.0 to 7.5 by adding 6 ml of 3.33M NaOH and stirring with a magnetic stirrer. Nickel and cobalt were precipitated as hydroxides according to Equation 2 and Equation3.

$$NiSO_4 + 2\,NaOH \rightarrow Na_2SO_4 + Ni(OH)_2 \quad (2.)$$

$$CoSO_4 + 2NaOH \rightarrow Na_2SO_4 + Co(OH)_2 \quad (3.)$$

RESULTS AND DISCUSSIONS

In this study, optimum parameters for nickel and cobalt production from limonitic type lateritic ores by using atmospheric pressure sulfuric acid leaching process and pug- roast-leaching process were investigated.

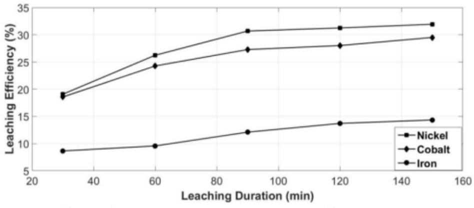

Fig. 3 Effect of leaching time on leaching efficiencies

In the atmospheric pressure sulfuric acid leaching experiments, the effects of leaching time, leaching temperature, acid concentration, particle size and pulp density on the leaching efficiencies were investigated. The effects of leaching time on nickel (Ni), cobalt (Co) and iron (Fe) leaching efficiencies are given in Figure 3. Significant increases in leaching efficiency were observed until leaching time reached 90 minutes. Further increase in leaching time had only a minor effect on leaching efficiencies. Therefore, 90 minutes was chosen as the optimum leaching time.

The effects of acid concentration on nickel (Ni), cobalt (Co) and iron (Fe) leaching efficiencies are given in Figure 4. Nickel, cobalt and iron leaching efficiencies were significantly increased until the acid concentration increased to 150 g/l. When acid concentration increased up to 200 g/l, increase in leaching efficiencies of nickel and cobalt slowed down. On the other hand, leaching efficiency of iron increased significantly. Since iron is not desired in the solution and higher iron causes higher cost of chemicals used for neutralization and precipitation processes, 150 g/l was determined as the optimum acid concentration.

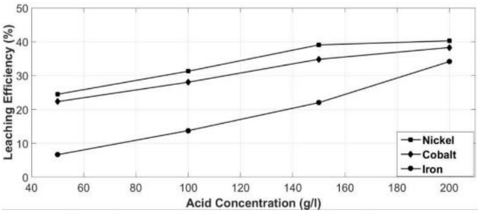

Fig. 4 Effect of acid concentration on leaching efficiencies

Figure 5 show the effect of leaching temperature on nickel (Ni), cobalt (Co) and iron (Fe) leaching efficiencies. As it can be seen on Figure 5, leaching efficiencies for nickel, cobalt and iron increased significantly with increasing leaching temperature until 80°C. When leaching temperature rised above 80°C, leaching efficiency of iron showed an almost linear increase, but increase in the leaching efficiencies of nickel and cobalt slowed down. For this reason, 80°C was determined as optimum leaching temperature.

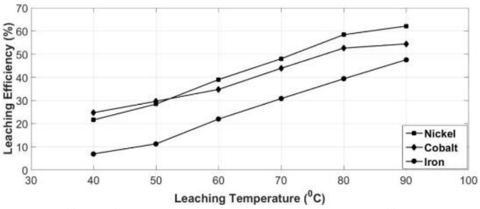

Fig. 5 Effect of leaching temperature on leaching efficiencies

Figure 6 illustrates the effect of particle size on nickel (Ni), cobalt (Co) and iron (Fe) leaching efficiencies. The reaction interface was increased with decreasing particle size and this resulted in higher leaching efficiencies. The increase in leaching efficiencies was not the same for three metals. As can be seen from Figure 6, cobalt leaching efficiency increased significantly when particle size decreased from 100 µm to 74 µm. This result shows that, among these three metals, kinetics is more important in cobalt leaching. Kinetic limitations can be reduced by decreasing the grain size in cobalt leaching. The main targeted metal nickel's leaching efficiencies were not significantly affected by grain size falling below 74 µm. Therefore, the optimum grain size was determined as 74 µm.

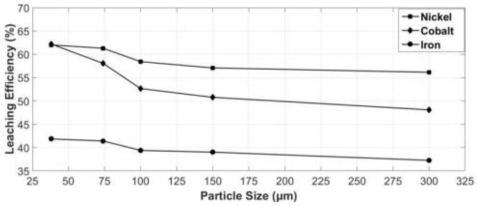

Fig. 6 Effect of particle size on leaching efficiencies

The effect of pulp density on leaching efficiencies was investigated for various acid and water ratios. As it can be seen in Figure 7, leaching efficiencies decreased when pulp density exceeded 10 %. Figure 7 also illustrates that nickel leaching efficiency decreased significantly when pulp density increased from 10 % to 20 % for 150 g/l acid concentration, which was determined as the optimum acid concentration. Since nickel is the main target metal, the optimum pulp density was determined as 10 %.

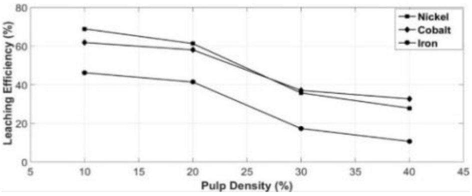

Fig. 7 Effect of pulp density on leaching efficiencies for 150 g/l acid concentration

In the pug-roast-leaching experiments, the effects of acid concentration, roasting time, roasting temperature, pulp density and leaching time (applied after roasting) on leaching efficiencies were investigated. In the acid concentration experiments, the required amount of H_2SO_4 was calculated stoichiometrically based on the quantitative analysis of the ore. 0.7-1.0-1.5-2.0 acid (g)/ore (g) ratios were used in acid concentration experiments. Results are given in Figure 8. Acid concentration is considered as the most important parameter affecting roasting, and hence it also affects leaching efficiency. Theoretically, using sulfuric acid at a weight equivalent to 70 % by weight of the ore is enough for roasting. However, the results of the experiments showed that using sulfuric acid in an amount equal to 150 % of the ore weight is essential for transferring nickel and cobalt to solution. When the acid/ore ratio exceeded 1.5, there was no significant increase in the leaching efficiencies of nickel and cobalt, but there was an important increase in the leaching efficiency of iron. For this reason, the optimum acid/ore ratio was determined as 1.5. Also, it can be seen in Figure 8 that the increase in the acid/ore ratio affects the sulfation and transfer of the iron to the solution more than nickel and cobalt.

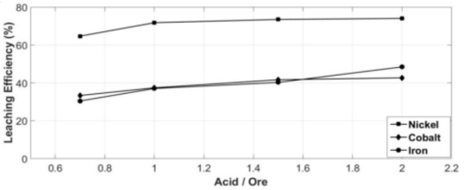

Fig. 8 Effect of acid concentration on leaching efficiencies in pugging process

After determining the optimum sulfuric acid quantity, the effect of roasting time on leaching efficiencies was investigated. Figure 9 shows the effect of roasting time on nickel (Ni), iron (Fe) and cobalt (Co) leaching efficiencies. The increase of roasting time had a slightly positive effect on nickel and cobalt leaching efficiencies. Dissolution of these metals was inhibited because of kinetic reasons. The amount of these two metals in the lateritic ore is relatively low and they show fine distribution within the ore. On the other hand, iron leaching efficiency was not affected by the increase in roasting time. As can be seen in Figure 9, there was no increase in leaching efficiencies for roasting times exceeding 30 minutes. So, 30 minutes was determined as optimum roasting time.

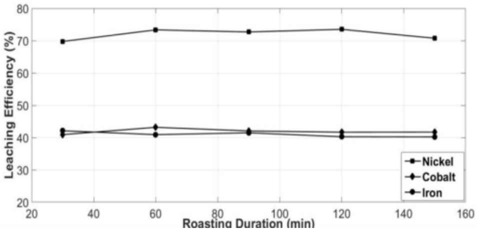

Fig. 9 Effect of sulfation roasting time on leaching efficiencies

After determining the optimum acid concentration and roasting time, the optimum roasting temperature was investigated. Figure 10 shows the effect of roasting temperature on leaching efficiencies of nickel, iron and cobalt. Leaching efficiencies increased with rising roasting temperature. It is known that 575°C is the decomposition temperature of iron sulfates and 675°C is the decomposition temperature of the nickel sulfates [19]. However, even if these temperatures are not reached, it has been seen in the previous studies that sulfates begin to decompose after 450°C, therefore leaching efficiencies start to decrease. Therefore, temperatures over 300°C were not used in the experiments and 300°C was determined as the optimum roasting temperature.

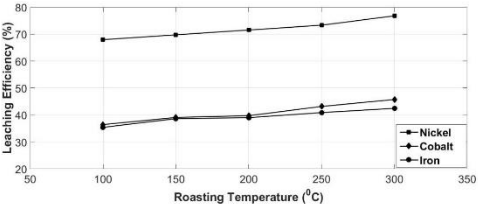

Fig. 10 Effect of sulfation roasting temperature on leaching efficiencies

After sulfation roasting was carried out with optimum conditions, the effect of leaching time on leaching efficiencies was investigated. Leaching was executed after roasting, and water was used in this process. Figure 11 shows the effect of leaching time on the leaching efficiencies of nickel, iron and cobalt. Leaching efficiencies increased until leaching time reached 30 minutes. A further increase in leaching time had no significant effect on leaching efficiencies. Therefore, 30 minutes was determined as the optimum leaching time.

After roasting, an intermediate product which consists of mixed sulphates was formed. This intermediate product was weighed, and water was added at various amounts to obtain different pulp densities. Figure 12 shows the effect of pulp density on leaching efficiencies of nickel, iron and cobalt. Leaching efficiencies decreased with increasing pulp density.

Decreases in nickel and cobalt leaching efficiencies were higher when compared to the leaching efficiency of iron. Although maximum leaching efficiencies of nickel and cobalt were achieved at 0.1 g/ml pulp density, optimum pulp density was determined as 0.125 g/ml, because the leaching efficiency of iron was affected more negatively with the increase in pulp density when compared to cobalt and nickel.

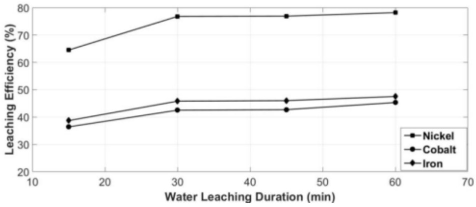

Fig. 11 Effect of leaching time on leaching efficiencies

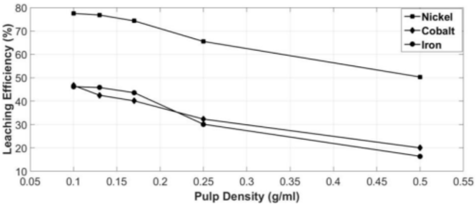

Fig. 12 Effect of pulp density on leaching efficiencies

Leaching efficiencies obtained in the two processes for optimum conditions were compared and it was found that nickel leaching efficiency was higher and iron leaching efficiency was lower for the pug-roast-leaching process as indicated on Figure 13. Therefore, iron removal and mixed hydroxide precipitation processes were applied to the samples subjected to the pug-roast-leaching process.

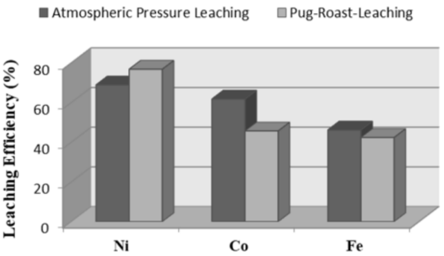

Fig. 13 Comparison of Processes for Leaching Efficiencies

After the pug-roast-leaching process was carried out at optimum conditions, iron removal was applied to the solution. The efficiency of this process was measured using AAS analysis. After this process was completed, nickel and cobalt were precipitated by mixed hydroxide precipitation process. The efficiency of the mixed hydroxide precipitation was calculated from AAS analysis data.

In the iron removal process, 40 ml of H_2O_2 was added drop by drop to 200 ml of pregnant solution for oxidation. Then, 3.33M NaOH was added to this mixture and it was observed that iron in the solution was precipitated. During this process, the effect of pH value on iron removal efficiencies and also nickel loss were investigated. Solid and liquid phases were separated by using filtration. When the AAS analysis which was performed after the iron removal process and the AAS analysis which was performed before the iron removal process were compared, it was found that 98.6% of iron was precipitated on pH value 4.0 as indicated on Figure 14. However, it was seen that 17.2% of the nickel was lost together with the precipitate in the iron removal process. As it can be seen on Figure 14, nickel loss percentage increases over 3.5 pH value while iron removal efficiency does not significantly. Optimum pH value for iron removal process was determined as 3.5. Nickel partially precipitates together with iron which precipitates as very fine-grained iron hydroxide compound. That would be the reason for the loss of nickel.

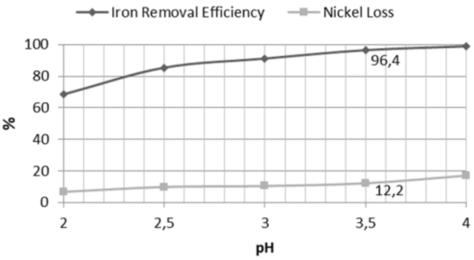

Fig. 14 Effect of pH to Iron Removal Efficiency and Nickel Loss

In the mixed hydroxide precipitation process, initially, the pH of the solution was increased to 7.5 with 8 ml of 3.33M NaOH addition. Solid which contains nickel and cobalt hydroxides and residual iron hydroxide, and liquid which contains a trace amount of manganese, magnesium and residual nickel and cobalt were separated from each other by filtration. Then filter cake was dissolved in 15 ml HCl + 5 ml HNO_3. Afterward, AAS analysis was conducted on the two solutions. According to the results, it was seen that 90.8% of nickel and 75.2% of cobalt were precipitated.

CONCLUSION

In this study, nickel and cobalt were extracted from limonite type lateritic nickel ores, which were taken from Manisa Caldag region of Turkey, by using atmospheric pressure sulfuric acid leaching and pug-roast-leaching processes. In atmospheric pressure sulfuric acid leaching experiments, the effects of leaching time, acid concentration, particle size and pulp density on leaching efficiencies were investigated. According to the results, optimum parameters were determined as; 150 g/l H_2SO_4 concentration, 80°C leaching temperature, 90 minutes of leaching time, 74 µm particle size and 10% pulp density. Leaching efficiencies of 68.9% Ni and 61.8% Co were obtained at optimum conditions. On the other hand, 46.2% of the iron in the ore was dissolved. In pug-roast-leaching experiments, the effects of acid concentration, roasting temperature, roasting time, pulp density and leaching time (applied after roasting) on leaching efficiencies were investigated. Optimum conditions were determined to be: 1.5 acid (H_2SO_4)/ore ratio, 300°C roasting temperature, 30 minutes of roasting time, 0.125 g/l pulp density and 30 minutes of leaching time. Leaching efficiencies of 76.8% Ni, 45.7% Co and 42.4% Fe were obtained with optimum parameters. When atmospheric pressure sulfuric acid leaching and pug-roast-leaching processes were compared, it was seen that Ni leaching efficiency was nearly 8% higher and iron leaching efficiency was nearly 4% lower in pug-roast-leaching process. Lower iron leaching efficiency will result in less neutralization reagent and oxidant used in the iron removal process, and this will reduce operating costs. Moreover, the atmospheric pressure sulfuric acid leaching process is completed in 90 minutes, while the pug-roast-leaching process takes 60 minutes. Shortening the duration by 33% is very important for industrial scale production.

The leaching efficiencies obtained seem to be a little bit low and the main reason for this would be the lack of acid regeneration during leaching. The efficiencies could be increased by returning the acid which contains nickel and cobalt to the beginning of the leaching or pugging processes. If acid conversion and sulfuric acid production are done at the end of the pug-roast leaching process, nickel and cobalt leaching efficiencies would increase and metal loss would be minimized.

According to the results obtained in this study, nickel and cobalt production from limonite type lateritic nickel ores, which were taken from Manisa Caldag region of Turkey can be carried out efficiently by hydrometallurgical processes. When we consider the importance of the materials such as stainless steels, high quality alloyed steels and nickel and cobalt based super alloys, this ore and these methods are significant for the production and industrial scale production can be integrated to the parameters that have been optimized in this study.

REFERENCES

1. X. Zhai, Y. Fu, X. Zhang, L. Ma, and F. Xie, *Hydrometallurgy*, 99(3-4), 2009, S189–S193. https://doi.org/10.1016/j.hydromet.2009.08.006.

2. Y. V. Swamy, B. B. Kar, and J. K. Mohanty, *Hydrometallurgy*, 69(1-3), 2003, S89–S98. https://doi.org/10.1016/S0304-386X(03)00027-6.

3. R. G. McDonald and B. I. Whittington, *Hydrometallurgy*, 91(1-4), 2008, S35–S55. https://doi.org/10.1016/j.hydromet.2007.11.009.

4. W. R. Liu *et al.*, *Trans. Nonferrous Met. Soc. China (English Ed.*, 20, 2010, no. SUPPL.1, pp. S82–S86. https://doi.org/10.1016/S1003-6326(10)60017-9.

5. M. Landers, R. J. Gilkes, and M. Wells, *Appl. Clay Sci.*, 42(3-4), 2009, S615–S624. https://doi.org/10.1016/j.clay.2008.05.002.

6.S. Kursunoglu, Z. T. Ichlas, and M. Kaya, *Trans. Nonferrous Met. Soc. China (English Ed.*, 28(8), 2018, S1652–S1659. https://doi.org/10.1016/S1003-6326(18)64808-3.

7. S. Kursunoglu, Z. T. Ichlas, and M. Kaya, *Hydrometallurgy*, 171, 2017, S179–S184. https://doi.org/10.1016/j.hydromet.2017.05.013.

8. S. Kursunoglu and M. Kaya, *Int. J. Miner. Process.*, 150, 2016, S1–S8. https://doi.org/10.1016/j.minpro.2016.03.001.

9. S. Kaya and Y. A. Topkaya, *Miner. Eng.*, 24(11), 2011, S1188–S1197. https://doi.org/10.1016/j.mineng.2011.05.004.

10. B. B. Kar, Y. V. Swamy, and B. V. R. Murthy, *Hydrometallurgy*, 56(3), 2000, S387–S394. https://doi.org/10.1016/S0304-386X(00)00086-4.

11. B. B. Kar and Y. V. Swamy, *Miner. Eng.*, 13(14-15), 2000, S1635–S1640. https://doi.org/10.1016/S0892-6875(00)00147-3.

12. I. Girgin, A. Obut, and A. Üçyildiz, *Miner. Eng.*, 24(7), 2011, S603–S609. https://doi.org/10.1016/j.mineng.2010.10.009.

13. M. N. El Hazek, F. Y. Ahmed, M. A. El Kasaby, and R. M. Attia, *Hydrometallurgy*, 90(1), 2008, S34–S39. https://doi.org/10.1016/j.hydromet.2007.09.009.

14. Y. Chang, X. Zhai, B. Li, and Y. Fu, *Hydrometallurgy*, 101(1-2), 2010, S84–S87. https://doi.org/10.1016/j.hydromet.2009.11.014.

15. H. Basturkcu, M. Achimovičová, M. Kaňuchová, and N. Acarkan, *Hydrometallurgy*, 181, 2018, S43–S52. https://doi.org/10.1016/j.hydromet.2018.08.016.

16. H. Basturkcu, N. Acarkan, and E. Gock, *Int. J. Miner. Process.*, 163, 2017, S1–S8. https://doi.org/10.1016/j.minpro.2017.04.001.

17. C. H. Köse and Y. A. Topkaya, *Miner. Eng.*, 24(5), 2011, S396–S415. https://doi.org/10.1016/j.mineng.2010.11.010.

18. S. Çetintaş, U. Yildiz, and D. Bingöl, *J. Clean. Prod.*, 199, 2018, S616–S632. https://doi.org/10.1016/j.jclepro.2018.07.212.

19. M. A. R. Önal and Y. A. Topkaya, *Hydrometallurgy*, 142, 2014, S98–S107. https://doi.org/10.1016/j.hydromet.2013.11.011.

20. E. Büyükakinci and Y. A. Topkaya, *Hydrometallurgy*, 97(1-2), 2009, S33–S38. https://doi.org/10.1016/j.hydromet.2008.12.014.

21. J. Esther, A. Pattanaik, N. Pradhan, and L. B. Sukla, *Mater. Today Proc.*, 30(1), 2020, S351–S354. https://doi.org/10.1016/j.matpr.2020.02.167.

22. S. Ilyas, R. R. Srivastava, H. Kim, N. Ilyas, and R. Sattar, *Sep. Purif. Technol.*, 232, 2020, S115971. https://doi.org/10.1016/j.seppur.2019.115971.

23. S. Mondal, B. Paul, V. Kumar, D. K. Singh, and J. K. Chakravartty, *Sep. Purif. Technol.*, 156, 2015, S827–S837. https://doi.org/10.1016/j.seppur.2015.11.007.

24. C. T. Harris, J. G. Peacey, and C. A. Pickles, *Miner. Eng.*, 24(7), 2011, S651–S660. https://doi.org/10.1016/j.mineng.2010.10.008.

25. M. H. Morcali, L. T. Khajavi, and D. B. Dreisinger, *Int. J. Miner. Process.*, 167, 2017, S27–S34. https://doi.org/10.1016/j.minpro.2017.07.012.

26. L. Y. Wang and M. S. Lee, *Int. J. Miner. Process.*, 166(1), 2017, S45–S52. https://doi.org/10.1016/j.minpro.2017.07.004.

27. M. Landers, R. J. Gilkes, and M. Wells, *Appl. Clay Sci.*, 42(3-4), 2009, S615–S624. https://doi.org/10.1016/j.clay.2008.05.002.

28. M. Landers and R. J. Gilkes, *Appl. Clay Sci.*, 35(3-4), 2007, S162–S172. https://doi.org/10.1016/j.clay.2006.08.012.

29. L. Y. Wang and M. S. Lee, *J. Mol. Liq.*, 240(1), 2017, S345–S350. https://doi.org/10.1016/j.molliq.2017.05.103.

30. A. Van der Ent, A. J. M. Baker, M. M. J. V. Balgooy, and A. Tjoa, *J. Geochemical Explor.*, 128(1), 2013, S72–S79. https://doi.org/10.1016/j.gexplo.2013.01.009.

31. G. Dublet *et al.*, *Geochim. Cosmochim. Acta*, 95(1), 2012, S119–S133. doi:10.1016/j.gca.2012.07.030

32. S. Sarbishei and L. Tafaghodi Khajavi, *Fuel*, 280, 2020, S118-S148. https://doi.org/10.1016/j.fuel.2020.118648.

33. G. Dublet, F. Juillot, G. Morin, E. Fritsch, D. Fandeur, and G. E. Brown, *Geochim. Cosmochim. Acta*, 160(1), 2015, S1–S15. https://doi.org/10.1016/j.gca.2015.03.015.

34. G. Senanayake, G. K. Das, A. De Lange, J. Li, and D. J. Robinson, *Hydrometallurgy*, 152(1), 2015, S44–S54. https://doi.org/10.1016/j.hydromet.2014.12.001.

35. X. Zhai, Y. Fu, X. Zhang, L. Ma, and F. Xie, *Hydrometallurgy*, 99(3-4), 2009, S189–S193. https://doi.org/10.1016/j.hydromet.2009.08.006.

36. M. L. Gillmore *et al.*, *Mar. Pollut. Bull.*, 152, 2020, S110-S886. https://doi.org/10.1016/j.marpolbul.2020.110886.

ACTA METALLURGICA SLOVACA
2021, VOL. 27, NO. 1, 23-27

RESEARCH PAPER

THEORY AND TECHNOLOGY OF MANUFACTURING A FERROALLOY FROM CARBON FERROCHROME DUSTS

Viktor Shevko[1], Yevgeniy Afimin[1], Gulnara Karataeva[1], Alexandra Badikova[1*], Timur Ibrayev[2]

[1] M. Auezov South Kazakhstan University, Department of Metallurgy, Tauke Khan avenue 5, Shymkent 160012, Kazakhstan

[2] Shymkent Smelting LLP, Kapal Batyr street 30, Shymkent 160000, Kazakhstan

*Corresponding author: sunstroke_91@mail.ru, tel.: +7-701-529-50-29, Department of Metallurgy, M. Auezov South Kazakhstan University, 160012, Shymkent, Kazakhstan

Received: 06.11.2020
Accepted: 13.01.2021

ABSTRACT

The article contains the research results of obtaining a ferroalloy from a carbon ferrochrome dust containing 30,2 % of $Cr2O3$, 23.4 % of $SiO2$, 32.7 % of MgO, 5.0 % of FeO, 1.6 % of CaO, 4.5 % of $Al2O3$, 2.3 % of C, and 0.3 % - others. The studies were carried out by a thermodynamic modeling method using the HSC-6.0 software package (Outokumpu) based on the principle of the Gibbs energy minimum, the Box-Hunter rototable planning technique and electric melting of the dust in an arc furnace. It was found that the interaction of the dust with carbon under equilibrium conditions and in the presence of iron leads to formation of $Cr4C$ (T>1000°C), $Cr3C2$, $Cr7C3$, Cr (T>1100°C), FeSi (T>1300°C), SiC (T>1400°C), SiOg and Si (T>1500°C). In the temperature range of 1745-1900°C and in the presence of 18-34% of carbon and 8% of iron of the dust mass, the resulting ferroalloy contained 18.5-25.2% of Si and 46.8-49.4% of Cr (in this case the silicon extraction degree into the alloy was 60.0-64.4%, the chromium one – 99.8%). When the electrosmelting the granulated dust together with coke and steel shavings, the chromium extraction degree into the alloy was 98.5-99.4%, the silicon one – 53.7-57.0%; the obtained ferroalloys containing 18.3-21.9% of silicon and 45.6-53.6% of chromium meet the requirements to FeCrSi23-grade ferrosilicochromium.

Keywords: ferroalloy, dust, carbon ferrochrome, electrosmelting, ferrosilicochromium, thermodynamic

INTRODUCTION

Kazakhstan is one of the largest producers of ferrochrome in the world (13% of world production) [1]. The share of ferrochrome in Kazakhstan accounts for 86.8% (2019) of the total production of ferroalloys in the country [2].

The ferroalloy production is characterized by dust formation [3].The quantity and chemical composition of the dust depend on the alloy type, its production technology, the electric furnace design and power, the furnace bath temperature, pressure in the under-roof furnace space, the electrode arrangement, the electrical regime (in particular, for each ferroalloy, there is a limit value for the phase voltage, the excess of which leads to a sharp increase in the dust content in the furnace gases), as well as on the heat resistance of the ore and reducing [4]. Dust in the ferroalloy furnaces is formed as a result of mechanical entrainment of raw material components and due to sublimation of metals, their oxides and sulfides. The specific dust yield also depends on the furnace design [4,5]. The dust yield at the smelting carbon ferrochrome ranges from 12 kg to 150 kg [5-8] per 1 tonne of the alloy. The dust contains 10-15% of SiO_2, 15-43.6% of Cr_2O_3, 13-33% of MgO, 3-8% of Al_2O_3, 0.2-4.5% of CaO, 4-6% of FeO, 1-1.2% of S, up to 6.2% of C.

The dust formed during the producing ferrochrome in electric arc furnaces contains various metals, such as chromium, zinc, iron, aluminum and magnesium. Some of these metals, for example chromium (VI), pose a threat to the environment and human life because of their toxicity [9]. Various studies have been conducted on the extraction of metals from dust, for example, the possibility of using vermiculite to remove Cr(VI) from fine-dispersed ferrochrome dust after its leaching in an aqueous solution [10], as well as the separation of chromium from industrial dusts by water ozonation [11]. To extract zinc from the ferrochrome dust collected in bag filters, a two-stage leaching procedure is proposed, which allows extracting zinc by 71.2% [12].

A hydrometallurgical method on the processing of carbon ferrochrome dust was suggested, which allows to obtain a chromium concentrate, followed by obtaining chromium metal by aluminothermic reduction [6]. The paper [13] describes the results of electric melting of high-carbon ferrochrome dusts (Aktobe Ferroalloy Plant, Aktobe, Kazakhstan) in a direct current arc furnace (DCAF-1). The recovery of chromium to chromium metal was 89.5%. The resulting alloy contained (wt.,%): Cr – 70.98; Fe-20.27; C – 8.09; Si – 0.61; S – 0.03; P – 0.02.

A research related to studying the possibility of using ferrochrome dust for production of concrete (partial replacement for conventional Portland cement) show that the addition of up to 40% of the dust and 7% of lime does not affect the properties of concrete (does not worsen or improve it) [14,15].

Due to its high fire resistance, the ferrochrome production dust can be used for manufacture of refractory materials [16], such as refractory bricks [17]. In order to recycle the waste formed at the production of high-carbon ferrochrome at the Aktobe Ferroalloy

DOI: 10.36547/ams.27.1.745

Plant, it is proposed to apply the bag filter dust to produce refractory materials for furnace lining [18].

The carbon ferrochrome dust is also used as a binder for the pelletizing chromium-containing ores (50% of the dust and 12% of a commonly used binder) [4, 19, 20] as well as at the manufacturing a refractory chromium oxide containing concentrate (95.8% of Cr_2O_3) [8].

In contrast to the well-known works, we suggest to use the carbon ferrochrome dust to produce high-quality ferroalloys containing Cr, Si and Fe.

MATERIAL AND METHODS

Subtitle of material and methods

The research was carried out using a thermodynamic modeling technique and experimental electric melting of the dust in a laboratory ore-thermal arc furnace. The thermodynamic modeling was performed using the HSC-6.0 software package (Outokumpu) [21], based on the minimum Gibbs energy principle. To calculate the equilibrium distribution degree of the dust elements (α_{el}, %), we developed an algorithm [22]. According to the algorithm, using the data about the quantitative distribution of substances obtained by means of an Equilibrium Compositions module of the HSC-6.0 software package, the equilibrium distribution degree of elements (α_{el}, %) is determined as a ratio of the mass of an element (kg) in the product ($G_{el(pr)}$) to the mass of the element (kg) in the initial system ($G_{el(init)}$) under the formula:

$$\alpha_{el} = \frac{G_{el(pr)}}{G_{el(init)}} \times 100 \tag{1.}$$

The mass of an element in the initial mixture ($G_{el(init)}$, kg) was calculated by the following way:

$$G_{el} = \frac{x \times A_{el}}{M_i} \times G_i \tag{2.}$$

where A_{el} – atomic mass of an element;

M_i – molecular weight of the initial substance;

G_i – mass of the initial substance, kg;

x – the number of kilo-atoms of an element in the initial substance.

The mass of an element in the products ($G_{el(pr)}$, kg) was calculated using the formula:

$$G_{el(pr)} = \frac{n \times A_{el}}{M_{i(pr)}} \times G_{i(pr)}, \tag{3.}$$

where A_{el} – atomic mass of an element; $M_{i(pr)}$– molecular weight of the product; $G_{i(pr)}$ – mass of the product, kg; n – the number of kilo-atoms of an element in the product.

After determination of $G_{el(pr)}$ and $G_{el(init)}$ the elements' equilibrium distribution degree was calculated under the formula (3). In addition, the effect of temperature and carbon amount on the formation of a ferroalloy and the silicon and chromium content in the resulting ferroalloy were determined.

The experimental installation is shown in figure 1.

Electric melting of a charge was carried out in a single-electrode arc furnace lined with chrome-magnesitebricks. The hearth electrode was made of a graphite block. A graphite crucible (d = 6 cm, h = 12 cm) was placed on the hearth. The space between the crucible and the lining was filled with graphite chips. The upper part of the furnace was closed with a removable cover with holes for the graphite electrode (d = 3 cm) and the gas outlet.

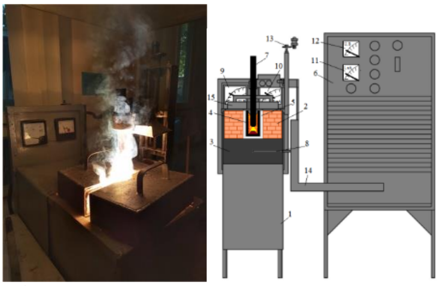

1 – furnace casing; 2 – chrome-magnesitelining; 3 – carbon graphite plate; 4 – graphite crucible; 5 – fine-crushed graphite; 6 – TAFH-1002 transformer; 7 – graphite electrode; 8 – lower current supply; 9-12 – ammeters and voltmeters; 13 – electrode movement mechanism; 14 – flexible part of a short network; 15 – furnace cover; I – general view; II – schemeof the furnace

Fig. 1 A laboratory single-electrode electric arc furnace

Before the melting, the crucible was heated with electric arc for 20-25 minutes at amperage of 250-300Aand voltage of 45-55V. A part of a charge (200-230 g) was loaded in the heated crucible. It was melted for 3-5 minutes, and then the remaining part of the charge (200-250 g) was loaded in the crucible and melted for the required time. The current during the melting was 350-450A and the voltage was 25-30V. Electricity to the furnace was supplied through a TAFH-1002 transformer. The required power was maintained by means of a thyristor regulator. The amperage was monitored by a Tangen 42L6 ammeter (the accuracy class is 1.5), and the voltage by a Chint 42L6 voltmeter (the accuracy class is 1.5). After termination of the electric melting, the furnace was cooled for 6 hours. Then the graphite crucible was taken out of the furnace and broken. The alloy was weighed and analyzed using a scanning electron microscope to determine the metals and carbon content. The coke before the charging were crushed to a fraction of 0.5-1.5 cm and dried at 120 °C. The dried components were pelletized in a plate-type granulator in the presence of a binder (bentonite clay). The pellets (d = 1 cm), dried at 120-140 ^{0}C, had the strength of 5-7 kg per a pellet and withstood 5 drops from a height of 1 m.

According to the data of the test chemical laboratory of the Aktobe Ferroalloy Plant (a branch of JSC "TNC Kazchrome"), the ferroalloy dust contains 21-35% of Cr_2O_3, 6-20% of SiO_2, 14-31% of MgO, 3.7-5.7% of Al_2O_3, 7-9% of FeO, 0.6-7.4% of CaO, 3-6% of C, 0.3-1% of S.

During the experiments we used the dust containing 30,2% of Cr_2O_3, 23.4% of SiO_2, 32.7% of MgO, 5.0% of FeO, 1.6% of CaO, 4.5% of Al_2O_3, 2.3% of C, 0.3% of others, as well as coke (85,7% of C, 5.2% of SiO_2, 2.1% of Fe_2O_3, 2.0% of Al_2O_3, 1.6% of CaO, 0.4% of MgO, 0.8% of H_2O, 5.0% of FeO) and steel shavings (2,1% of C, 0,4% of S, 97.1% of Fe, 0.4% of others).

RESULTS AND DISCUSSION

Subtitle of results and discussion

The effect of carbon and temperature on the quantitative (kg) distribution of substances containing chromium and silicon at the interaction of the dust formed at the manufacturing ferrosilicochrome (hereinafter referred to as dust) with carbon (18% of the dust mass) in the presence of iron (8% of the dust mass) is represented in figure 2.

As follows from the figure, the reduction products in the system under consideration are chromium carbide, chromium, iron silicide, iron monoxide, silicon and calcium carbide, which begin to form at the following temperatures: Cr_4C – 1000 °C, Cr_3C_2, Cr_7C_3 and Cr – 1100 °C, FeSi – 1300 °C, SiC – 1400 °C, SiO_g

and Si – 1500 °C. Chromium is completely reduced at 1400 °C, and silicon at 2100 °C.

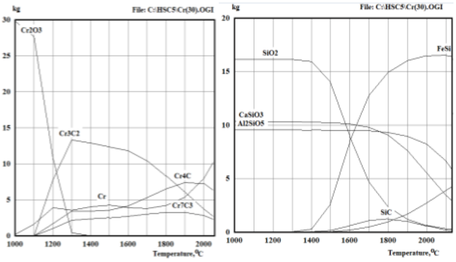

Fig. 2 Temperature effect on the quantitative distribution of chromium (I) and silicon (II) containing substances in a system of dust – C – Fe

Figure 3 shows the effect of temperature (from 1400 to 1900 °C) and amount of carbon (18% and 34% of the dust mass) on the equilibrium silicon transition degree (*αSi*) and chromium and silicon content in the resulting alloy (*C_{Cr}*, *C_{Si}*, %). It can be seen that a high *αSi* (>55%) is at the temperature of more than 1700-1800 °C. An increase in the carbon amount from 18 to 34% increases *αSi* from 55 to 61% (at 1800 °C). At the constant carbon quantity (18 or 34%) an increase in the temperature from 1400 to 1800 °C leads to an increase in the silicon extraction degree into the alloy and the silicon concentration in it. In this case, the chromium concentration in the alloy decreases.

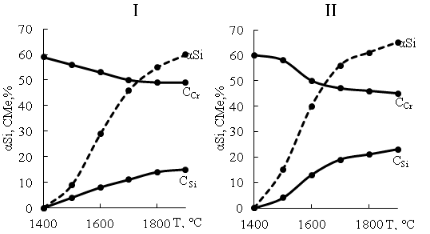

I – 18% of carbon; II – 34% of carbon

Fig. 3 The temperature and carbon amount effect on *αSi, C_{Si}* and *C_{Cr}*

The chromium concentration achieves its maximum value of 59.8% at 1400 °C and 18-34% of carbon; the maximum silicon content is 16.4-23.0% at 1800-1900 °C and 34% of carbon. The change in the concentration of elemental chromium and its carbides is shown in figure 4.As follows from figure 4, an increase in the temperature from 1400 to 1900 °C changes the concentration of chromium-containing substances. So, if at 1400 °C and 18% of carbon C_{Cr3C2}>C_{Cr}>C_{Cr4C}>C_{Cr7C3}, then at 1800 ^{0}C C_{Cr3C2}>C_{Cr4C}>C_{Cr}>C_{Cr7C3}. At 34% of carbon and 1800 °C the sequence of changes in the concentrations is different – C_{Cr3C2}>C_{Cr}>C_{Cr4C}>C_{Cr7C3}.

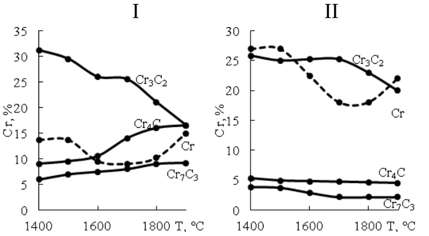

I – 18% of carbon; II – 34% of carbon

Fig. 4 The temperature and carbon amount effect on the concentration of chromium and its carbides in the ferroalloy

The pattern of temperature and carbon amount effect on *αSi, C_{Si}* and *C_{Cr}* (table 1) was obtained on the basis of the data of figure 3 and the results of the additional study conducted by a planning method [23].

Table 1 A planning matrix and indicators of temperature (T, °C) and carbon (C, %) influence on the silicon transition degree and the silicon and chromium concentrations in the alloy

№	Variables				α_{Si}, %	C_{Si}, %	C_{Cr}, %
	Code kind		*Natural kind*				
	X1	*X2*	*C,%*	*T, °C*			
1	+1	+1	31.7	1856	62.6	21.0	46.2
2	-1	+1	20.3	1856	59.1	20.8	48.7
3	+1	-1	31.7	1644	48.0	15.9	48.6
4	-1	-1	20.3	1644	38.3	13.0	50.8
5	+1.41	0	34	1750	60.2	22.0	45.9
6	-1.41	0	18	1750	51.6	17.4	49.8
7	0	+1.41	26	1900	60.9	20.8	47.0
8	0	-1.41	26	1600	34.5	11.3	51.3
9	0	0	26	1750	55.0	19.9	48.0
10	0	0	26	1750	54.3	20.3	48.4
11	0	0	26	1750	55.6	19.5	47.6
12	0	0	26	1750	54.8	19.7	47.9
13	0	0	26	1750	55.4	20.1	48.3

Based on the table data and using [23], the following adequate regression equations were obtained:

$$\alpha Si=-1197{,}08+1{,}274\cdot T+4{,}245\cdot C-3{,}2\cdot 10^{-4}\cdot T^2+1{,}539\cdot 10^{-2}\cdot C^2-2{,}56\cdot 10^{-3}\cdot T\cdot C \quad (4.)$$

$$C_{Si}=-477.76+0.56\cdot T-1{,}957\cdot C-1{,}59\cdot 10^{-4}\cdot T^2+1{,}17\cdot 10^{-3}\cdot C^2+1{,}24\cdot 10^{-3}\cdot T\cdot C \quad (5.)$$

$$C_{Cr}=60.608+1{,}49\cdot 10^{-3}T-0{,}993\cdot C-6{,}76\cdot 10^{-6}\cdot T^2+1{,}77\cdot 10^{-2}\cdot C^2-1{,}24\cdot 10^{-4}T\cdot C \quad (6.)$$

On the basis of the regression equations and according to the method [24], three-dimensional and planar images of the temperature and carbon effect on *αSi, C_{Si},C_{Cr}* were constructed (figure 5).

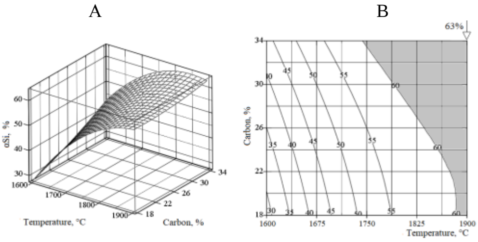

Numbers by lines – *αSi*, %

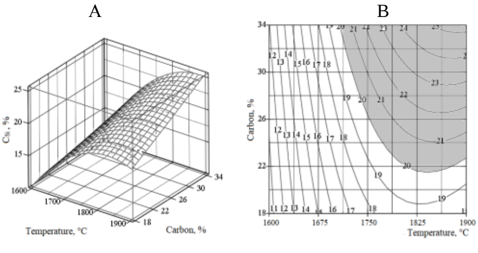

Numbers by lines – *C_{Si}*, %

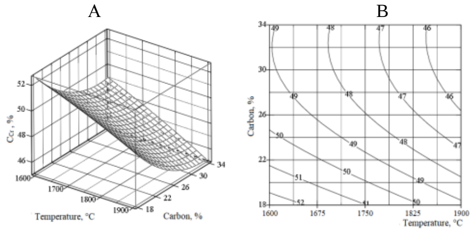

Numbers by lines – C_{Cr}, %
A – three-dimensional images; B – one-dimensional image
Fig. 5 Temperature and carbon effect on αSi(I),C_{Si}(II),C_{Cr}(III)

Judging by the figures, αSi is from 60 to 63.0% for the temperature range of 1745-1900 °C and the carbon amount of 18-34% (the shaded area of figure 5 (I, B); C_{Si} is from 20 to 23.2% at 1710-1900 °C and 19.8-34% of carbon. As follows from figure 5 (III, B), the chromium concentration of ≥50% in the alloy is at 18-24.3% of carbon in the temperature interval of 1600-1830 °C. At the higher temperature (1900 °C) and 34% carbon content, the chromium concentration in the alloy decreases to 46.6%. Figure 6 represents the combined information about the temperature and carbon influence on the technological parameters of the dust processing, provided that αSi is more than 60%.

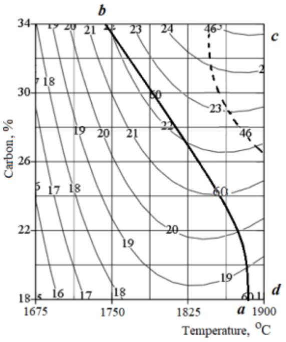

αSi (▬), C_{Si}(---), C_{Cr}(- - -)
Fig. 6 Temperature and carbon amount effect on the technological parameters of processing the ferrosilicochrome dusts

The process parameters for the boundary points of the *abcd* area, where $\alpha Si \geq 60\%$, are shown in table 2.

Table 2 The process technological parameters in the boundary points

Point in fig. 5	T, ^{0}C	Carbon, %	αSi, %	C_{Si}, %	C_{Cr}, %	Alloy grade
a	1880	18	60.0	18.7	49.4	FeCrSi23
b	1745	34	60.0	21.9	47.4	
c	1900	34	64.4	25.2	46.8	
d	1900	18	60.6	18.5	49.2	

The data of table 2 show that in the equilibrium conditionsat 1745-1900 ^{0}C and 18-34% of carbon (αSi is 60-64. 4%), the resulting ferroalloy containing 18.7-25.2% of silicon and 46.8-49.4% of chromium corresponds to the FeCrSi23-grade ferrosilicochrome [25].
The results of electric melting of the charge consisting of the dust, coke and steel shavings (8% of the dust mass) are shown in table 3. Photos of several alloys and the content of elements in them are shown in figures 7-8.

Table 3 Resultsof electric melting of ferrochrome dusts

Experiment #	Carbon, % of the dust mass	αSi, %	αCr, %	C_{Si}, %	C_{Cr}, %
1	20	53.7	96.8	22.6	41.26
2	24	54.6	98.9	21.9	45.6
3	28	53.9	99.3	19.5	49.9
4	32	55.8	98.5	18.4	53.0
5	36	57.0	99.4	18.3	53.6

I – alloy # 1; II – alloy # 4
Fig. 7 Photographs of the resulting ferroalloys

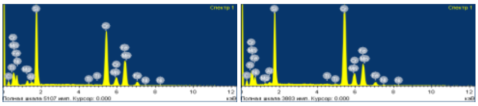

I – alloy # 1 II – alloy # 4

Element	Cr	Si	Fe	Mg	Mn	Ni	Al	Ti	C
Mass fraction in the alloy # 1, %	41.26	22.60	31.8	1.61	1.37	0.27	0.71	0.27	4.2

Element	Cr	Si	Fe	Mg	Mn	Ni	Al	Ti	C
Mass fraction in the alloy # 4, %	53.28	18.40	21.98	0.28	2.04	0.48	0.41	0.28	3.14

Fig. 8 Energy-dispersion spectra and elemental composition of the alloys composition made by the scanning electron microscope

The ferroalloys produced (alloys 2-5) in accordance with [25] belong to ferrosilicochromium of the FeCrSi23 grade, for which the chromium concentration is ≥45%, and the silicon content is in the interval of 18-28%.

CONCLUSION

The results obtained at the processing of the dusts formed at the manufacturing carbon-containing ferrochrome allowed to draw the following conclusions:
1. In the equilibrium conditions:
   - interaction of the dusts with carbon in the presence of iron occurs with the formation of Cr_4C (T>1000 ^{0}C), Cr_3C_2, Cr_7C_3, Cr (T>1100 ^{0}C), FeSi (T>1300 ^{0}C), SiC (T>1400 ^{0}C), SiO_g and Si (T>1500 ^{0}C);
   - an increase in the amount of carbon from 18 to 34% of the dust mass leads to an increase in the silicon and chromium transition degree into the alloy and the silicon concentration in the alloy;
   - in the temperature interval of 1745-1900 ^{0}C and in the presence of 18-34% of carbon and 8% of iron of the dust mass, a ferroalloy is produced, which contains 18.5-25.2% of Si and 46.8-49.4% of Cr (the silicon extraction degree in the alloy is 60.0-64.4%, one for Cr is 99.8% and more).
2. When the electro smelting the granulated dust together with coke and steel shavings, the extraction degrees of chromium and silicon were 98.5-99.4% and 53.7-57.0%, respectively; the resulting ferroalloys containing 18.3-21.9% of silicon and 45.6-53.6% of chromium corresponds to ferrosilicochrome of FeCrSi23 grade.

REFERENCES

1. P.H. Kumar, A. Srivastava, V. Kumar, M.R. Majhi, V.K. Singh: Implementation of industrial waste ferrochrome slag in conventional and low cement castables: Effect of microsilica addition, Journal of Asian Ceramic Societies, 2(2), 169-175, 2014. https://doi.org/10.1016/j.jascer.2014.03.004.

2. [12.10.2020], https://www.zakon.kz/4985129-kazahstan-vhodit-v-troyku-mirovyh.html.

3. S.B. Stark: *Dust collection and gas cleaning in metallurgy*, Moscow: Metallurgy, 1977, 328.

4. A.M. Kasimov, A.I. Rovensky, B.N. Maksimov: *Dust and gas emissions in the production of the main types of ferroalloys*, Moscow: Metallurgy, 1988, 110.

5. I.D. Kashcheev, V.I. Zhuchkov, O.V. Zayakin: Forming and Utilizing of Ferrochromium Production Waste, Russian Internet Journal of Industrial Engineering, 7(3), 2019, 6. http://doi.org/10.24892/RIJIE/20190307.

6. P.P. Lazarevskiy, R.A. Gizatulin, Yu.E. Romanenko, D.V. Valuev, A.V. Valueva, A. Serikbol: Extraction of Chromium from Carbon Ferrochromium Residual Wastes, IOP Conference Series: Materials Science and Engineering, 91 2015, 8. https://doi.org/10.1088/1757-899X/91/1/012038.

7. M.I. Gasik, V.A. Zubov: *Electrometallurgy ferrosilicon*, Dnepropetrovsk: System technologies, 2002, 704.

8. P.P. Lazarevsky, Yu.E. Romanenko: Obtaining chromium concentrate for chemical enrichment by processing dust from carbon ferrochrome production, In.: *Innovations in materials science and metallurgy*, Yekaterinburg: Ural Publishing House, 2015, 16-20.

9. V.A. Uzbekov, A.A. Mamyrbayev, E.Zh. Otarov, S.A. Ibrayev, N.Z. Perepichko: Assessment of risk of exposure to human of the chromium compounds during chromium ore mining and ferrochromium gaining, *Medicine and Ecology*, 1(70), 2014, 24-27.

10. M.M. Delphin, M.G.Andrie: Stabilization of Cr(VI) from fine ferrochrome dust using exfoliated vermiculite, Journal of Hazardous Materials 223-224, 2012, 46-52. http://dx.doi.org/10.1016/j.jhazmat.2012.04.046.

11. Y. Staden, J.P. Beukes, P.G. Zyl, J.S. Toit, N.F.Dawson: Characterisation and liberation of chromium from fine ferrochrome waste materials, Minerals Engineering, 56, 2014, 112-120. https://doi.org/10.1016/j.mineng.2013.11.004.

12. J.G. Strobos, J.F. Friend: Zinc recovery from baghouse dust generated at ferrochrome foundries, Hydrometallurgy, 74 (1–2), 2004, 165-171. https://doi.org/10.1016/j.hydromet.2004.03.002.

13. O. Sariev, B. Kelamanov, Ye.Zhumagaliyev, S. Kim, A. Abdirashit, M. Almagambetov: Remelting the high-carbon ferrochrome dust in a direct current arc furnace (dcf), Metalurgija, 59(4), 2020, 533-536.

14. P.K. Acharya, S.K. Patro: Utilization of ferrochrome wastes such as ferrochrome ash and ferrochrome slag in concrete manufacturing, Waste Management & Research, 34, 2016. https://doi.org/10.1177/0734242X16654751.

15. P.K. Acharya, S.K. Patro: Effect of lime and ferrochrome ash (FA) as partial replacement of cement on strength, ultrasonic pulse velocity and permeability of concrete, Construction and Building Materials, 94, 2015, 448–457. https://doi.org/10.1016/j.conbuildmat.2015.07.081.

16. I.D. Kascheev, V. I. Zhuchkov, O.V. Zayakin: Forming and Utilizing Ferrochromium Production Waste, Materials Science Forum, 989, 2020, 492–497. https://doi.org/10.4028/www.scientific.net/msf.989.492.

17. R.U. Kozhamuratov, R.Z. Safarov, Yu.G. Nosenko, Zh.K. Shomanova: Ferroalloy production waste disposal,In.: *Global Science and Innovations 2017*, Bursa: Eurasian Center of Innovative Development, 2017, 207-213.

18. A.K. Zhunusova, A.R. Mamonov, A.K. Zhunusov: Recycling of ferrochrome aspirational dust, Science and technology of Kazakhstan, 3-4, 2016, 66-70.

19. G.V. Horoshun, S.N. ,Fedoseev: Processing of secondary raw materials and application in metallurgy, In.: *Ecology and safety in the technosphere: modern problems and solutions*: collection of proceedings of the All-Russian scientific and practical conference, Tomsk: Tomsk Polytechnic University, 2016, 66-69.

20. A.K. Zhunusov, N.K. Kulumbaev, Zh.O. Nurmaganbetov, L.B. Tolymbekova: Production of chrome ore pellets from fine waste, Science and technology of Kazakhstan, 3, 2016, 39-44.

21. A. Roine, J. Mansikka, T. Kotiranta, P. Bjorklund, P. Lamberg: *HSC Chemistry 6.0 User's Guide*, Outotec Research Oy, 2006.

22. V.M. Shevko, G.M. Serzhanov, G.E. Karataeva, D.D. Amanov: *Calculation of the equilibrium distribution of elements in relation to the HSC-5.1 software package*, Certificate for an object protected by copyright of the Republic of Kazakhstan No. 1501 dated January 29, 2019.

23. S.L. Akhnazarova, V.V. Kafarov: *Experiment optimization methods in chemical technology*, Moscow: Higher school, 1985, 327.

24. V.F. Ochkov: *Mathcad 14 for students, engineers and designers*, St. Petersburg.: BHV- Petersburg, 2009, 512.

25. State standard 11861-91 (ISO 5449-80). *Ferrosilicochromium. Specification and conditions of delivery*, Moscow: Standards Publishing House, 2003, 10.

ACTA METALLURGICA SLOVACA
2021, VOL. 27, NO. 1, 28-31

RESEARCH PAPER

CHARACTERISTIC OF INTERFACE BIMETAL ALUMINUM-COPPER FOR BIMETAL BUSHING PRODUCED BY CENTRIFUGAL CASTING

Nugroho Santoso[1], Bambang Suharnadi[1], Benidiktus Tulung Prayoga[1], Lilik Dwi Setyana[1]*

[1] Department of Mechanical Engineering, Vocational College, Universitas Gadjah Mada, Yogyakarta, 55281, Indonesia

*Corresponding author: lilikdwi_s@ugm.ac.id, tel.: +628562856934, Vocational College, Universitas Gadjah Mada, 55281, Yogyakarta, Indonesia

Received: 13.11.2020
Accepted: 16.12.2020

ABSTRACT

Bimetallic is a type of metal composite that combines two metals that form a metallurgical bond. The manufacture of bimetallic bushings by centrifugal casting has not been developed much. Recently, there is no recommendation yet for optimum temperature and speed of rotation to produce bimetallic bushings. The research was conducted to determine the rotation of the mold in centrifugal casting so as to produce a well-integrated interface. The materials used for the manufacture of bimetallic bushings are aluminum and copper. Aluminum was melted at a temperature of 750 °C, while copper was melted at 1200 °C. Molten metal was pouring alternately. First, aluminum was poured into the mold, and then after the aluminum temperature reached 400 ºC, copper was poured into the mold to form a bushing aluminum-copper bimetallic. The molten metal was poured into a rotating sand mold with a constant filling speed of about 0.15 kg s^{-1}. The variations of the rotational speed of the mold were 250, 300, and 350 rpm. The result shows that the interface's width increases as the mold rotation increases during the pouring process. Interface hardness and wear are increased compared to the base metal. Hence, centrifugal casting with 350 rpm is recommended for aluminum-copper bimetal bushing applications.

Keywords: Bushing bimetal; Centrifugal casting; Aluminum-Copper; Interface

INTRODUCTION

The centrifugal casting principle applies forces generated from the centripetal acceleration of a rotating mold [1]. Centrifugal casting produces a product with accurate dimensions and limited gas porosity [1,2]. These characteristics are caused by the distribution of molten metal into the mold cavity, which uses forces resulted from the centripetal acceleration of a mold rotation. The centrifugal force is influenced by the rotational speed, radius, metal density [1], and gating system [3]. The non-pressurized system, with reduced turbulence and the increasing cross-sectional area towards the mold cavity, can increase the mechanical properties [4]. Moreover, to improve the average bending strength can be done by enlarging the vortex runner diameter in the gating system [5]. The pressure distribution controlled by rotational speed affects the porosity, which can be reduced by the rotational speed of more than 180 rpm [6]. Furthermore, the quality of casting products depends on the combination of the rotational speed, runner design, and gating system [7, 8].

Bimetallic is a type of metal composite that combines two metals that form a metallurgical bond (metal bond) [9]. The purpose of bimetallic production is to make an integrated component consisting of two metals, but each metal still has its unique properties [10]. The presence of metal bonds on the surface of the two metals increases the components' mechanical properties. The two metals complement each other in mechanical, chemical, and physical properties [11].

Bimetallic composites can be made by gravity casting [12] or centrifugal casting [10]. The manufacture of bimetallic composites by casting produces a cohesive compound and diffusion of the metal interface during pouring, resulting in a high bond strength [13]. One of the current developments of bimetal is to manufacture bushing products. Making bushings using the gravity casting method will produce low-density products with cast defects [12]. Meanwhile, the manufacture of bushing by centrifugal casting will create products with accurate dimensions, smooth surface, less gas porosities, and faster freezing [2].

Centrifugal casting utilizes the force generated by the centripetal acceleration of a rotating mold to distribute molten metal into the mold [1]. High rotation reduces the number of product defects [14]. Castings with high temperatures require higher rotational speeds to avoid sliding. Meanwhile, the low casting temperature will cause the casting surface to be rough, and the gas porosity appears. Casting temperature affects the rate of freezing and the amount of segregation that occurs [10].

Evaluation of the copper-aluminum bimetallic interface shows that the primary layer's freezing time is calculated based on the Chornief equation [10]. The pouring of the second metal liquid after a different time will change the components' interface temperature. Interfacial diffusion capability and hardness depend on the temperature of the copper and aluminum when casting in the mold. The intermetallic structure, which is brittle, will decrease if the pouring temperature is low. Metallurgical bonds will become strong if the pouring temperature is suitable and reduced impurities or metal oxides [10]. Defects that form in the bimetallic are due to a delay when pouring molten copper after solidification of the aluminum. This causes the formation of metallurgical bonds at the interface to improperly formed [9].

The strength of the aluminum-copper bond at the interface has resulted from bonding the intermolecular and intermetallic compounds of the two metals being held together. The higher the

DOI: 10.36547/ams.27.1.756

casting temperature will increase the bond strength of the two metals interface. However, if the temperature is too high, it will result in the emergence of a new phase, which is brittle and lower strength [10].

The interface bond between metals in centrifugal casting is influenced by rotation speed [9]. One of the bonds formed at the interface is the quasicrystalline and intermetallic phases, which are embedded in the Al-FCC matrix. This phase has stability and high mechanical strength (4-7 times from before) [15]. The mechanical, physical, and chemical properties of the intermetallic phase are very different from those of the two constituent metals. The development of bimetal bushings with centrifugal casting continues, but there is no recommendation yet for suitable temperature and speed to produce a sound product. Analysis and evaluation are carried out on product and interface defects to have high hardness and wear resistance. The research is conducted to determine the rotation of the mold in the centrifugal casting in order to produce appropriate integration at the interface.

MATERIAL AND METHODS

The materials used in this research were aluminum and copper. The main compositions of aluminum and copper were shown at **Table 1** (tested by a spectrometer with IK 5.4-1-1 method).

Table 1 Chemical composition of materials (wt.%)

Alloy	Composition (wt.%)						
	Al	Cu	Si	Fe	Mn	Zn	Ni
Al	92.33	0.48	4.93	0.68	0.21	0.98	0.03
Cu	0.09	99.63	0.02	0.01	0.01	0.12	0.06

Aluminum-copper bimetallic bushing was produced by vertical centrifugal casting. Aluminum was melted at a temperature of 750 ºC, while copper was melted at a temperature of 1200 ºC. The molten metal was poured into a rotating sand mold with a constant filling speed of about 0.15 kg s^{-1}. First, aluminum was poured into the mold, and then after the aluminum temperature was 400 ºC, copper was poured into the mold to form aluminum-copper bimetallic in the form of a bushing. Molten metal pouring was carried out alternately. The variations of the rotational speed of the centrifugal casting mold were 250, 300, and 350 rpm. The schematic product of bushing can be seen in **Fig. 1**. Bushings had 35 mm and 25 mm diameters for outer and inner, respectively, with a height of 30 mm. The thickness of aluminum and copper is 2.5 mm each.

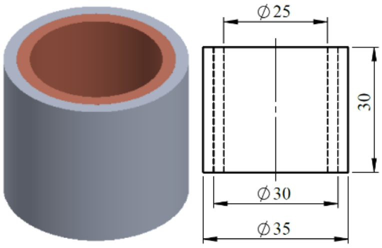

Fig. 1 The schematic product of bushing

The observations carried out in this research included microstructures in the interface of bimetal. The microstructure characterization was analyzed using a metallurgical microscope (PME 3, Olympus, Japan) and SEM-EDS (Quanta x50 SEM Series). Preparation was done with #180 to #1000 sandpapers to obtain a smooth surface, then metal polished. While to uncover the microstructure (etching process), a hidroflouride (HF) was used in aluminum, while an HNO_3 60% was used in copper.

The tests done in this research included hardness and wear tests. The hardness was obtained in the interface between aluminum and copper samples using a hardness micro Vickers tester (HMV-M3, Shimadzu, Japan). The distance among each test point of the hardness test was 50 µm with a load of 50 gf, which is hold for 5s. The wear test was carried out on the interface between aluminum and copper samples using universal wear (Riken Ogoshi's, Tokyo, Japan) with a load of 6.36 kgf as far as 15 m.

RESULTS AND DISCUSSION

Results

Fig. 2 shows the microstructure at the bimetal interface with variations in rpm.

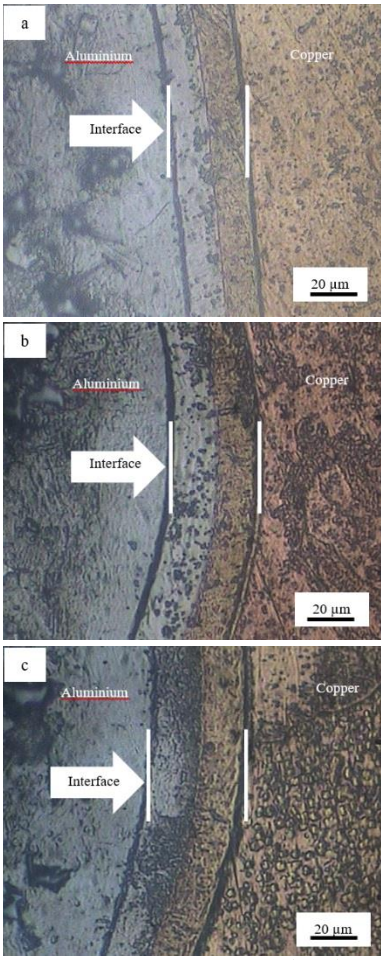

Fig. 2 The microstructure at the bimetal interface of Al-Cu, produced with 250 rpm (a); 300 rpm (b); and 350 rpm (c)

Based on the observations, it can be seen that all products with variations in rpm occur Al-Cu intermetallic compounds (IMCs). It is similar with previous research [10, 16]. The thickness of IMCs increases in line with the increase of the mold rotation.

The thicknesses of IMCs for the products with the rotation of 250, 300, and 350 rpm were 33, 37, and 41 µm, respectively.

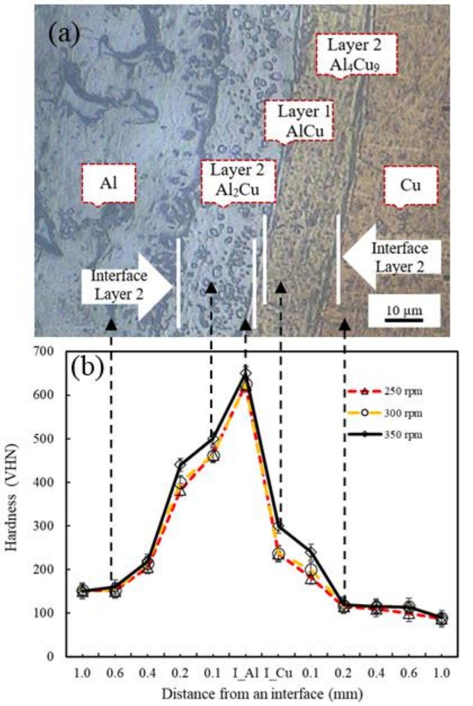

Fig. 3 (a) Microstructure at the interface with inference component, (b) the hardness of each interface

The microstructure at the interface with the inference component (based on SEM-EDS) can be seen in **Fig. 3(a).** Based on the observation, in the Al_2Cu interface (layer 2) and Al_4Cu_9 are formed, while at the AlCu interface (layer 1) is formed. The results of this observation are similar to previous studies [16]. The width of interface layer 2 of Al_2Cu and Al_4Cu_9 regions is almost the same for about 20 µm. While the width of the interface layer 1 is about 2 µm.

The hardness test results in the interface area can be seen in **Fig. 3 (b).** The hardness at interface layer 2 and layer 1 is increased compared to the hardness of the base metal. The hardness of aluminum (150 VHN), which is made at 350 rpm, increases at the Al_2Cu interface layer (500 VHN) then reaches the highest hardness at the AlCu interface layer (624 VHN). The hardness drops on the interface layer Al_4Cu_9 (300 VHN), then decreases again in the copper area (114 VHN). The trend of hardness looks similar between specimens with variations in rpm. The hardness is particularly affected by the kind of phase of the microstructure [17].

Fig. 4 shows the wear of the bimetal interface. The wear of aluminum, Al_2Cu, Al_4Cu_9 interface and copper are 1.7E-07, 9.7E-08, 1.3E-07, and 6.6E-07 mm^{3}kg^{-1}m^{-1} respectively. The wear interface is 1.7 times higher than aluminum and 6.8 times higher than copper.

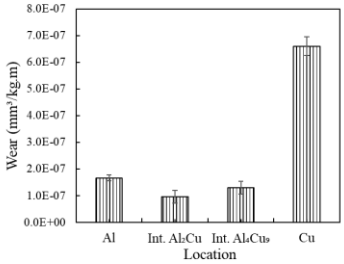

Fig. 4 The wear of bimetallic interface

Discussion

The aluminum-copper bimetallic of interface bonding made by centrifugal casting in variations of rpm occurs well. The interface width increases in line with the increase of mold rotation. The bimetallic interface widths made with rpm 250, 300, and 350 are 33, 37, and 41 µm, respectively. The molten metal pressure increases due to the centrifugal and tangential force acting on molten metal when entering the mold [3,18]. The high rotation during pouring increases the driving force of the molten metal into the mold. This condition results in better bonding at the interface. Interfaces are formed because of the bonds between atoms so that no new phases are formed [10].

From the microstructure observations in several places, it was seen that there were impurities in the interface area caused by metal oxides and protective oxides of the two materials. Based on observations, there are more impurities in the Al_4Cu_9 interface. There are correlations between the microstructure with the mechanical properties [19]. The pressure of the molten metal cannot remove the metal oxide, so that there is no special bond at the interface. If there are impurities, the two metals separate, and a diffusion bond does not form between them. The least impurities at the interface occur in bushings made at 350 rpm. The rotational speed of the mold when pouring increases the liquid pressure distributed into the mold [1]. This reduces the number of product defects [14], one of which is oxide impurities. The hardness of the interface area is higher than that of the constituent metals. The hardness of aluminum and copper at a distance of 0.4 mm is the same as the hardness of the base metal. The hardness of the interface increased up to 650 VHN (≥ 4 times base metal). The higher the rotation of the mold when pouring causes the hardness at the interface to be higher. Increased hardness happens due to the formation of hard aluminum carbides.

The increase of wear on the interface area (layer 2) is caused by the formation of hard Al_2Cu, AlCu, and Al_4Cu_9. However, higher hardness does not always lead to better wear resistance. Hardness is should not necessarily be considered the most critical factor in assessing the wear resistance of a material [20]. There is a correlation between wear behavior with surface topography [20]. However, because the surface topography is prepared in similar conditions, hardness is a major factor in wear resistance.

CONCLUSION

The conclusions of this research are:

1. The width of the interface increases as the mold rotation increases during the pouring process.
2. The interface hardness and wear are increased compared to the base metal.
3. Centrifugal casting with 350 rpm is recommended for aluminum-copper bimetal bushing applications.

Acknowledgments
We thank the Department of Mechanical Engineering, Vocational College, Universitas Gadjah Mada for testing and observation equipment.

REFERENCES

1. W.S. Ebhota, A.S. Karun, F.L. Inambao: International Journal of Materials Research, 107(10), 2016, 1-10. https://doi.org/10.3139/146.111423.
2. S. Wu, Q. Xu, X. Xue: Advanced Materials Research, 317-319, 2011, 456-459. https://doi.org/10.4028/www.scientific.net/ AMR.317-319.456.
3. L.D. Setyana, M. Mahardika, Sutiyoko, Suyitno: Acta Metallurgica Slovaca. 25(3), 2019, 193-202. https://doi.org/10.12776/ams.v25i3.1315.
4. O. Akinlabi, A. Ayodele: Acta Metallurgica Slovaca, 21(2), 2015, 135-141, https://doi.org/10.12776/ams.v21li2.567.
5. R. Ahmad, M.Y. Hasyim: Archives of Metallurgy and Materials. 56(4), 2011, 991-997. https://doi.org/10.2478/v10172-011-0109-6.
6. Y. Ling, J. Zhou, H. Nan, L. Zhu, Y. Yin: Journal of Materials Processing Technology, 251, 2018, 295-304. https://doi.org/10.1016/j.jmatprotec.2017.08.025.
7. P. Suwankan, N. Sornsuwit, N. Poolthong: Key Engineering Materials, 659, 2015, 647-651. https://doi.org/10.4028/www.scientific.net/KEM.659.647.
8. B.H. Hu, K.K. Tong, X.P. Niu, I. Pinwill: Journal of Materials Processing Technology, 105(1-2), 1999, 128-133. https://doi.org/10.1016/S0924-0136(00)00546-X.
9. S. Pandey, P. Kumar, S.K. Jha, and A.K. Bharat: ELK Asia Pacific Journals, 2017, 1-6.
10. J. Nazari, M. Yousefi, A. Kerahroodi, B. Mofrad, and A. Abhari: International Journal of Materials Lifetime, 1(1), 2015, 20-28. https://doi.org/10.12691/ijml-1-1-4.
11. M. Abbasi, and J. Hejazi: The Sixth Annual Seminar of Iranian foundry society, Iran University of Science and Technology, 1994, 1-15.
12. L. Changyun, W. Haiyan, W. Shiping, X. Lei, W. Kuangfei, and F. Hengzhi: Rare Metal Materials and Engineering, 39(3), 2010, 388–392
13. C. Nerl, M. Wimmer, H. Hoffmann, E. Kaschnitz, F. Langbein, and W. Volk: Journal of Materials Processing Technology, 214(7), 2014, 1445-1455. https://doi.org/10.1016/j.jmatprotec.2014.02.018.
14. L. Jia, D. Xu, M. Li, J. Guo, and H. Fu: Metals and Materials International, 18(1), 2012, 55–61
15. G.Y. Koga, A.M.B. Silva, W. Wolf, C.S. Kiminamia, C. Bolfarini, and W.J. Botta: Journal of Materials Research and Technology, 8(2), 2019, 2092-2097. https://doi.org/10.1016/j.jmrt.2018.12.022.
16. W. Jiang, F. Guan, G. Li, H. Jiang, J. Zhu, Z. Fan: Materials and Manufacturing Processes, 34(9), 2019, 1016-1025. https://doi.org/10.1080/10426914.2019.1615084.
17. S. Darmo, L. D. Setyana, Tarmono, N. Santoso: IOP Conf. Series: Materials Science and Engineering, 384, 2018, 1-4. https://doi.org/10.1088/1757-899X/384/1/012017.
18. L.D. Setyana, M. Mahardika, Suyitno: Acta Metallurgica Slovaca, 26(3), 2020, 132-137. https://doi.org/10.36547/ams.26.3.535.
19. J. Bidulska, R. Bidulsky, M. A. Grande, T. Kvackaj: Materials, 12(22), 2019, 3724. https://doi.org/10.3390/ma12223724.
20. R. Bidulský, M.A. Grande: Powder Metallurgy, 59(2) 2016, 121-127. https://doi.org/10.1179/1743290115Y.0000000022.

ACTA METALLURGICA SLOVACA
2021, VOL. 27, NO. 1, 32-35

RESEARCH PAPER

MATHEMATICAL EQUATION FOR IMPURITY DISTRIBUTION AFTER SECOND PASS OF ZONE REFINING

Milan Skrobian[1]*, Rudolf Pernis[2]

[1] Inoval – Slovak Academy of Sciences, Priemyselna 525, 96501 Ziar nad Hronom, Slovakia,

[2] Farmet s.r.o, Robotnicka 4334, 01701 Povazska Bystrica, Slovakia

*Corresponding author: milan.skrobian@savba.sk, +421918725083, Inoval – Slovak Academy of Sciences 96501 Ziar nad Hronom, Slovakia

Received: 27.12.2020
Accepted: 08.01.2020

ABSTRACT

A mathematical equation has been derived that describes impurity distribution in ingot after second pass of zone refining. While an exponential impurity distribution is calculated by a simplified model after first pass, second pass is described by mixed linear - exponential model. Relationship of transformed impurity concentration is constant over whole length of semi-infinite ingot for first pass. However, it has linear trend for second pass. Last part of molten zone at infinity solidifies differently and can be described mathematically as directional crystallization. A mathematical tool devised for second pass of zone refining can be tried to be used for derivation of functions of more complex models that would describe impurity distribution in more realistic way compared to simplified approach. Such models could include non-constant distribution coefficient and/or shrinking or widening molten zone over a length of ingot.

Keywords: zone refining; second pass; mathematical description of impurity distribution

INTRODUCTION

A distribution of impurities between liquid and solid phase during crystallization was recognized many years ago. These phenomena were already mentioned by Nerst in his paper about theory of the kinetics of heterogeneous reactions in 1904 [1].

A zone refining (zone melting) technique is known almost one century. It is based on a different concentration of impurity in solid and liquid at their phase boundary. According to Feigelson first reported use of zone melting was by Kapica in 1928 [2 and citation thereof].

Among other scientists W. G. Pfann worked intensively on theory and practice of zone melting and other improved techniques of this kind. He describes them in his book [3]. When ingot with evenly distributed impurity over its whole volume is treated by zone refining, an impurity accumulates - when distribution coefficient is less than one – in melt. Mathematical equation describing distribution of impurity after first pass can be written in a form

$$c_{s1}(x) = c_0 + c_0 \cdot (k-1).e^{\frac{-k.x}{h}} \qquad (1.)$$

where “$c_{s1}(x)$” is concentration of impurity in solid phase after first pass, “c_0“ is initial concentration of evenly distributed impurity, “k” is distribution coefficient (ratio of impurity concentration in solid and liquid phase), “h” is width of molten zone and “x” is distance from beginning of ingot. Equation (1) holds when width of molten zone is constant during zone melting, cross-section area is constant, “k” keeps constant, no volume changes take place during solidification, mixing of melt is perfect and no diffusion takes place in solid phase. An above equation is valid for full ingot length except for last molten zone which solidifies fractionally [3]. Equation (1) is sometime ascribed to Pfann, however he gives credit for derivation of this equation to W. T. Read [4].

In a chapter about multi-pass zone melting in [3] Pfann mentions *“It would be most helpful to have a general equation that expresses solute concentration as a function of distance, for any number of passes through an ingot of specified length. No such equation has been derived. While the concepts of zone refining are simple, it is apparently difficult to describe multi-pass operations mathematically.“* Therefore several mathematical methods were devised to cope with this problem, e.g. [5-10]. They are, in principle, iterative numerical methods.

Situation with mathematical solution of zone melting has changed when powerful computer become readily available. Specific simulation software can be written and run where dynamic changes during zone melting can be analyzed [11-13 and citations thereof]. Although simulations are helpful, data need to be fed into software which is specific to the analyzed parameters.

METHODS

Mathematical description of impurity distribution during second pass of zone refining

The details of method for evaluation of mathematical equations describing impurity distribution after second pass of zone refining is shown in Appendix.

Integral material balance equation of zone refining for second and higher passes was “resistant to solution” for almost 70 years. Finally, application of multidisciplinary approach and transformation of integral equation into its differential form proved fruitful leading to an analytical solution.

DOI: 10.36547/ams.27.1.808

RESULTS AND DISCUSSION

Resulting equation of impurity distribution after second pass of zone refining is as follows:

$$\mathrm{c}_{s2}(x) = c_0 + c_0 \cdot (k-1) \cdot (2 - e^{-k}) \cdot e^{\frac{-k.x}{h}} + \frac{k}{h} \cdot c_0 \cdot (k-1) \cdot e^{-k} \cdot x \cdot e^{\frac{-k.x}{h}} \qquad (2.)$$

It can be written in more convenient way as:

$$\mathrm{c}_{s2}(x) = c_0 \cdot \left[1 + (a_{2,0} + a_{2,1} \cdot x) \cdot e^{\frac{-k.x}{h}}\right] \qquad (2a.)$$

where

$$a_{2,0} = a_{1,0} \cdot (2 - e^{-k}); \quad a_{2,1} = a_{1,0} \cdot \frac{k}{h} \cdot e^{-k}; \quad a_{1,0} = k - 1 \qquad (2b.)$$

Boundary concentration, i.e. concentration of impurity at position x=0 is k.c$_0$ for first pass. It is intuitively expected that boundary concentration should, at position x=0, equal k^2.c$_0$ for a second pass. However, as follows from equation (2) boundary concentration is different. Reason for it is as follows: impurity is evenly distributed over whole volume of ingot before first pass. Concentration of impurity in first molten zone with width of "h" is constant and equals c$_0$. Therefore ingot at position x=0 solidified with impurity concentration k.c$_0$. This is not valid for second pass since distribution of impurity over a volume of ingot is not constant anymore. It needs to be calculated as average concentration within molten zone as follows

$$c_{L2}(0 \div h) = \frac{1}{h} \cdot \int_0^h \left(c_0 + c_0 \cdot (k-1) \cdot e^{\frac{-k.t}{h}}\right) \cdot dt = \frac{1}{h} \cdot \left(c_0 \cdot h - c_0 \cdot \frac{h}{k} \cdot (k-1) \cdot e^{-k} + c_0 \cdot \frac{h}{k} \cdot (k-1)\right) \qquad (3.)$$

Ingot at boundary position x=0 solidifies as

$$c_{s2}(0) = k \cdot c_{L2}(0 \div h) = \frac{k}{h} \cdot \left(c_0 \cdot h - c_0 \cdot \frac{h}{k} \cdot (k-1) \cdot e^{-k} + c_0 \cdot \frac{h}{k} \cdot (k-1)\right) = c_0 + c_0 \cdot (k-1) \cdot (2 - e^{-k}) \qquad (4.)$$

Visualization of impurity distribution after second pass of zone refining

Surface of impurity concentration as a function of ingot length and distribution coefficient with dimensionless molten zone width of 0.2 is shown in Fig. 1. All units are arbitrary. Isolines of distribution coefficient run from left to right.

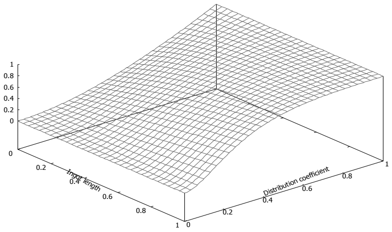

Fig. 1 Surface of impurity concentration as a function of ingot length and distribution coefficient [19]

Surface of impurity concentration as a function of ingot length and molten zone width with distribution coefficient of 0.2 is shown in Fig. 2. All units are arbitrary. It is seen in Fig. 2 that efficiency of impurity removal increases non-linearly with increasing molten zone width.

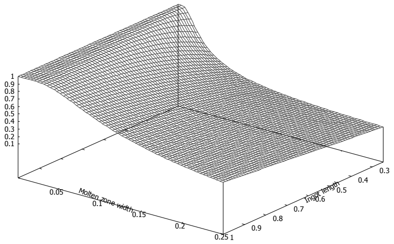

Fig. 2 Surface of impurity concentration as a function of ingot length and molten zone width [19]

Linearization of impurity distribution equations for first and second pass of zone refining

It is worth to note an interesting property of equation (1) and (2). When constant c$_0$ is subtracted from both sides, then both sides are divided by exponential member and initial impurity concentration the following relations hold:

$$\frac{c_{s1}(x) - c_0}{c_0 \cdot e^{\frac{-k.x}{h}}} = (k-1) \qquad (5.)$$

$$\frac{\mathrm{c}_{s2}(x) - c_0}{c_0 \cdot e^{\frac{-k.x}{h}}} = (k-1) \cdot (2 - e^{-k}) + \frac{k}{h} \cdot (k-1) \cdot e^{-k} \cdot x \qquad (6.)$$

Left side of equation (5) is constant for all values of independent variable (length of ingot) while in case of equation (6) it keeps linear trend. Note, that both sides of equation (5) and (6) are dimensionless.

CONCLUSION

A mathematical description of impurity distribution in ingot after second pass of zone refining has been derived using integral-differential approach. It is of mixed linear - exponential type.
From a mathematical point of view an integral – differential approach seems worth to try in search of equations for more complex models of zone refining such as non-constant distribution coefficient and/or shrinking or widening of molten zone over length of ingot.
Efficiency of impurity removal depends non-linearly on both distribution coefficient as well as molten zone width.

Acknowledgments: This paper has been written as follow up of EU project NFP 26220220069, activity Recycling of aluminium based composites.
Authors would like to thank to Associate Professor Ladislav Matejíčka, PhD for his valuable help when we have got stuck with solution of integral-differential equations.
One of the authors (M.S.) would like to dedicate this paper to his teacher, colleague and friend, now retired Associate Professor Jozef Ďurišin, PhD.

REFERENCES

1. W. Nerst: Theorie der Reaktionsgeschwindigkeit in heterogenen Systemen, Zeitschrift *für* Physikalische Chemie 47(1), 1904, 52. https://doi.org/10.1515/zpch-1904-4704.

2. R. S. Feigelson: Zone melting. In.: *Handbook of Crystal Growth*, ed. T. Nishinaga, Elsevier 2015. https://doi.org/10.1016/C2011-0-04376-4.
3. W. G. Pfann: *Zone Melting*. New York: John Wiley and Sons, 1958.
4. W. G. Pfann: Transactions of the American Institute of Mining and Metallurgical Engineers, 194, 1952, 747.
5. N. W. Lord: Transactions of the American Institute of Mining and Metallurgical Engineers, 197, 1953, 1531.
6. H. Reiss: Transactions of the American Institute of Mining and Metallurgical Engineers, 200, 1954, 1053.
7. K. S. Milliken: Journal of Metals, 7, 1955, 838.
8. J. Burris, C. H. Stockman, I. G. Dillon: Transactions of the American Institute of Mining and Metallurgical Engineers, 203, 1955, 1017.
9. J. L. Birman: Journal of Applied Physics, 26, 1955, 1195.
10. J. Braun, S. Marshall: British Journal of Applied Physics, 8, 1957, 157.
11. C. W. Lan, D. T. Yang: International Journal of Heat and Mass Transfer, 41(24), 1998, 4351-4373.
12. M. Nakamura et al.: Materials Transactions, 55(4), 2014, 664.
13. M. Ezheiyan, H. Sadeghi: Journal of Crystal Growth, 462, 2017, 1-5.
14. L. Kuchař, J. Drápala: *Metallurgy of pure metals* (in Czech), Košice: R. Kammel Foundation, 2000.
15. J. Škrášek, Z. Tichý: *Fundamentals of Applied Mathematics II* (in czech), SNTL Praha, 1986
16. L. Matejíčka: Mathematica Slovaca, 45(1), 1995, 91-103.
17. R. Harťanský, L. Matejíčka: Advances in Military Technology, 2, 2007, 5-11.
18. T. Harťanský, P. Mikuš, L. Maršálka, J. Slížik, L. Matejíčka: Universal Journal of Electrical and Electronic Engineering, 1(2), 2013, 52-57.
19. Gnuplot release 5.4.0, July 2020 (www.gnuplot.info)

Appendix

Evaluation of equation for second pass of zone melting

Distribution of impurity in zone refined ingot after first pass is mathematically described by eq. (1). Distribution of impurity during second pass is schematically shown in Fig. 3. This approach is based on material balance before and after second pass. A problem with end part of ingot can be solved mathematically as zone refining of semi-infinite sample. From a practical point of view, last ingot zone with width of "h" can be treated as fractional solidification. It accumulates high concentration of impurity.

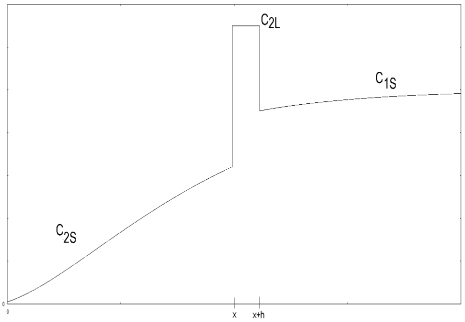

Fig. 3 Schematic distribution of impurity during second pass of zone refining

Material balance equation of impurity distribution for second pass that follows after first pass of zone refining can be written as follows

$$\int_0^x \mathrm{c}_{s2}(t)\cdot dt+\frac{h}{k}\cdot \mathrm{c}_{s2}(x)=\int_0^{x+h}\left(c_0+c_0\cdot(k-1)\cdot e^{\frac{-k.t}{h}}\right)\mathrm{dt} \tag{7.}$$

Right side of equation (7) can be evaluated as it is known function describing impurity distribution in ingot after first pass. Then a substitution $y=\int_0^x c2s(t)\cdot dt$ is applied. Second member of equation (7) on left side is thus $y'=\frac{dy}{dx}$ multiplied by $\frac{h}{k}$. Equation (7) can be written in a form

$$y+\frac{h}{k}\cdot y'=g(x) \tag{8.}$$

where

$$g(x)=\int\limits_0^{x+h}\left(c_0+c_0\cdot(k-1)\cdot e^{\frac{-k.t}{h}}\right)dt$$

Multiplying both sides of equation (7) by $\frac{k}{h}$ gives non-homogeneous linear differential equation of first order [15] in a form

$$\frac{k}{h}\cdot y+y'=\frac{k}{h}\cdot\left(L+c0\cdot x-M\cdot e^{\frac{-k.x}{h}}\right) \tag{9.}$$

where

$$L=c_0\cdot h+\frac{h}{k}\cdot c_0\cdot(k-1)$$
$$M=\frac{h}{k}\cdot c_0\cdot(k-1)\cdot e^{-k}$$

This kind of differential equations is used to solve integral-differential problems, e.g. [16-18] – integral equation (7) is transformed into differential form (9).
General solution of equation (9) is [15]:

$$y=\frac{1}{E(x)}\cdot\left(\int E(x)\cdot g(x)\cdot dx+C\right) \tag{10.}$$

$$where\ \ E(x)=e^{\int f(x)\cdot dx}=e^{\frac{k.x}{h}}$$

Integrating function g(x) in equation (8) and inserting result into equation (9) gives a solution

$$y=\left(L+c0\cdot x-\frac{h}{k}\cdot c0-\frac{k}{h}\cdot M\cdot x\cdot e^{\frac{-k.x}{h}}+C\cdot e^{\frac{-k.x}{h}}\right) \tag{11.}$$

Constants L and M are shown in equation (9), constant C need to be evaluated from boundary condition – equation (4). As follows from equations (7), (8) and (11), a final form of mathematical description of impurity distribution after second pass of zone refining can be written as

$$\mathrm{c}_{s2}(x)=\frac{dy}{dx}=c_0+c_0\cdot(k-1)\cdot\left(2-e^{-k}\right)\cdot e^{\frac{-k.x}{h}}+\frac{k}{h}\cdot c_0\cdot(k-1)\cdot e^{-k}\cdot x\cdot e^{\frac{-k.x}{h}} \tag{12.}$$

Verification of equation for second pass of zone refining

Check of correctness of derived equation (2) for second pass of zone refining is done by inserting of equation (1) and (2) into material balance equation (7):

$$\int_0^{x+h}\left(c_0+c_0\cdot(k-1)\cdot e^{\frac{-k.t}{h}}\right)\cdot dt=c_0\cdot(x+h)-\frac{h}{k}\cdot c_0\cdot(k-1)\cdot e^{-k}e^{\frac{-k.x}{h}}+\frac{h}{k}\cdot c_0\cdot(k-1) \tag{13a.}$$

$$\frac{h}{k}\cdot \mathrm{c}_{s2}(x)=\frac{h}{k}\cdot c_0+\frac{h}{k}\cdot P\cdot e^{\frac{-k.x}{h}}+\frac{h}{k}\cdot Q\cdot x\cdot e^{\frac{-k.x}{h}} \tag{13b.}$$

where

$$P = c_0 \cdot (k-1) \cdot (2 - e^{-k})$$
$$Q = \frac{k}{h} \cdot c_0 \cdot (k-1) \cdot e^{-k}$$

$$\int_0^x \mathrm{c}_{s2}(t) \cdot dt = c_0 \cdot x - \left(\frac{h}{k} \cdot P + Q \cdot \frac{h^2}{k^2}\right) \cdot e^{\frac{-k.x}{h}} - Q \cdot \frac{h}{k} \cdot x \cdot e^{\frac{-k.x}{h}} + \frac{h}{k} \cdot P + Q \cdot \frac{h^2}{k^2} \tag{13c.}$$

$$\frac{h}{k} \cdot P + Q \cdot \frac{h^2}{k^2} + \frac{h}{k} \cdot c_0 + c_0 \cdot x - Q \cdot \frac{h^2}{k^2} \cdot e^{\frac{-k.x}{h}} + \frac{h}{k} \cdot P \cdot e^{\frac{-k.x}{h}} - \frac{h}{k} \cdot P \cdot e^{\frac{-k.x}{h}} + \frac{h}{k} \cdot Q \cdot x \cdot e^{\frac{-k.x}{h}} - \frac{h}{k} \cdot Q \cdot x \cdot e^{\frac{-k.x}{h}} = c_0 \cdot (x+h) - \frac{h}{k} \cdot c_0 \cdot (k-1) \cdot e^{-k} e^{\frac{-k.x}{h}} + \frac{h}{k} \cdot c_0 \cdot (k-1) \tag{14.}$$

Last four members on left side of equation (14) cancel each other and remaining members on left and right side are equal – material balance equation (7) is satisfied.

ACTA METALLURGICA SLOVACA
2021, VOL. 27, NO. 1, 36-42

RESEARCH PAPER

SLURRY EROSION BEHAVIORS OF COPPER ALLOY BARREL OF MEASUREMENT WHILE DRILLING

Kang Jin Huang [1,2]*, Kun Xia Wei [1,2]*, Ke Zhang [3]†, Wei Wei [1,2]†, Qing Bo Du [1,2], Igor V. Alexandrov [2,4]†

[1] School of Materials Science and Engineering, Changzhou University, Changzhou 213164, P. R. China
[2] Jiangsu Key Laboratory of Materials Surface Science and Technology, Sino-Russian Joint Laboratory of Functional Nanostruc-tured Materials, Changzhou University, Changzhou 213164, P. R. China
[3] School of Metallurgical Engineering, Maanshan University of Technology, Maanshan 243032, P. R. China
[4] Department of Physics, Ufa State Aviation Technical University, 12 K. Marx St., 450008 Ufa, Russia

†Corresponding author. E-Mail: huzhude@yeah.net (K. Zhang), benjamin.wwei@163.com (W. Wei); IgorVAlexan-drov@yandex.ru (Igor V. Alexandrov), Tel.:+ 7-927-930-38-44, Department of Physics, Ufa State Aviation Technical University, 12 K. Marx St., 450008 Ufa, Russia
* These authors contributed equally to this work.

Received: 30.01.2021
Accepted: 06.02.2021

ABSTRACT

Measurement while drilling (MWD) has been widely used in petroleum drilling engineering because it can realize borehole trajectory monitoring and improve the drilling speed. However, the slurry erosion will deteriorate and shorten the life of MWD. A user-defined function (UDF) code was developed to calculate the particle properties (particle impact velocity, particle impact angle and particle impact number) and erosion depth to understand the erosion process. The results show that the Realizable κ-ε model can accurately predict the erosion profile and the erosion depth is consistent with the experiment results. Furthermore, high pressure will aggravate surface damage and expand the area of slurry erosion. It has been demonstrated that computational fluid dynamics (CFD) and experimental approach can be used to identify and explain the erosion mechanisms in different regions where the surface morphologies reveal four erosion patterns, namely, micro-cutting, cracks, pits and plastic deformation.

Keywords: MWD; Slurry erosion; Copper alloy; High pressure; CFD

INTRODUCTION

Measurement while drilling (MWD) is a kind of advanced drilling equipment, which has been widely applied because it can realize well trajectory monitoring and improve the drilling efficiency. In drilling operations, sand can provide the energy needed to break hard rock in a fast and cost-effective manner [1,2]. On the other hand, sand particles can bring about various problems, such as pressure drop, pipe blockage and erosion [3]. When solid particles in the fluid impact the copper alloy barrel of MWD, the equipment is prone to damage and failure, resulting in huge economic losses [4,5]. Therefore, in order to ensure the safe operation of MWD instrument and reduce the damage caused by the slurry erosion, an accurate erosion prediction is prerequisite.

The slurry erosion is a very complex phenomenon, which is affected by many factors such as particle impact velocity, particle impact angle and particle impact number and mechanical properties of barrel materials. For brittle materials [6], the erosion is mainly caused by cracking and peeling of barrel materials. For ductile materials [7-9], the erosion is generated by a series of repeated micro-plastic deformations.

In order to study the erosion rate and establish an erosion model, the Slurry Pot Erosion Test, Coriolis Test, Direct Impingement Jet Test and Pipe Loop Test [10-12] are provided to carry out standard experimental tests. DVN [13], E/CRC [14], Oka [15, 16], Grant and Tabakoff [17] erosion models are widely used owing to their relative simplicity and accuracy. However, in the fully automatic drilling environment, the determination of 3D erosion distribution is still challenging due to the long time and high cost of wall thickness monitoring. Computational fluid dynamics (CFD) can estimate particle microscopic characteristics that cannot be observed in the experimental methods. It is widely used for particle erosion prediction of related geometric shapes such as pipelines, tee pipes at sudden expansions and contractions [18-20]. However, no CFD investigation to date has been conducted to examine the slurry erosion behaviors of copper alloy barrel of WMD.

In the present, a combined numerical and experimental approach was used to investigate the erosion-induced surface evolution as well as the erosion mechanisms on the surface of the MWD barrel. CFD simulation results are helpful to make an insight into the particles impact on MWD barrel surface and the process of removing the material.

EXPERIMENTAL PARAMETERS

MWD testing system is mainly composed of ground equipment and downhole measuring instruments as shown in Fig. 1. Particles are irregularly shaped quartz sand with a density of 2450

DOI: 10.36547/ams.27.1.851

kg/m3 and the diameter in the range of 0.1~ 0.3 mm. The viscosity of the drilling fluid is 47.5CP and the density is 1325 kg/m3. Detailed composition of MWD barrel and experimental conditions are shown in Table 1 and Table 2. The relation between drilling fluid velocity u and fluid flow Q is referred to Eq. (1):

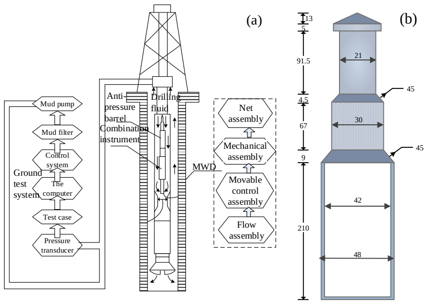

Fig. 1 Schematic of the experimental facility. (a) MWD testing system, (b) MWD barrel (mm)

$$u = \frac{C \cdot Q}{2.448 \times D^2} \tag{1.}$$

Q (L/s) is the fluid flow, C (3.117) is the empirical coefficient, and D (0.083 m) is the length scale of the fluid.

The total mass loss of MWD barrel was measured by the electronic balance. The local erosion depth and surface morphology were characterized by Super Depth 3D microscope (Keyence, VHX-6000).

Table 1 Experimental conditions

Conditions	Fluid flow (L/s)	Particle concentration (%)	Working pressure (MPa)	Testing time (h)
Test 1	55	0.5	0	200
Test 2	35	0.5	20	200
Test 3	15	0.5	20	200

Table 2 Physical properties and composition of Cu-Be (QBe2) alloy barrel of MWD

Material	Density (kg/m3)	Hardness (HB)	Young's modulus, E (GPa)	Poisson's ratio, υ	Yield strength (MPa)
QBe2	8300	213	128	0.27	195
Composition (wt. %)					
Be	Ni	Fe	Al	Si	Cu
1.86	0.21	0.07	0.03	0.02	Bal

NUMERICAL SIMULATION

3.1. Discrete phase model

The motion of particles is solved by Newton 's second law in the Lagrangian frame [21,22], which can be expressed as:

$$\frac{dv_p}{dt} = F_D(u - v_p) + g\frac{(\rho_p - \rho)}{\rho_p} + F \tag{2.}$$

$$F_D = \frac{18\mu C_D Re_p}{24\rho_p d_p^2}, \qquad Re_p = \frac{\rho d_p |u - v_p|}{\mu} \tag{3.}$$

where F_D is the drag force per unit particle mass. In this study, F represents the additional force and the pressure gradient per unit particle mass, g is the acceleration of gravity. v_p, ρ_p, d_p, C_D and Re_p are the particle velocity, density, diameter, drag coefficient and the Reynolds number, respectively.

The particle-wall interaction not only affects the velocity and angles, but also the trajectory of particles. The particle rebound model proposed by Forder et al [23] can be described as:

$$e_n = 0.988 - 0.78\theta + 0.19\theta^2 - 0.024\theta^3 + 0.027\theta^4 \tag{4.}$$

$$e_t = 1 - 0.78\theta + 0.84\theta^2 - 0.21\theta^3 + 0.028\theta^4 - 0.022\theta^5 \tag{5.}$$

where e_n and e_t are the normal and tangential restitution coefficients, respectively. θ (rad) is the particle impact angle.

3.2. Erosion model

Oka erosion model [15, 16] is obtained on the basis of a large number of erosion experiments. The relationship between $K(\alpha \cdot HV)^{k_1 b}$ and E_{90} at reference impact velocity can be derived based on Oka experimental results. The function of SiO_2~Cu is described as [16]:

$$K(\alpha \cdot HV)^{k_1 b} \approx 81.714(HV)^{-0.15} \tag{6.}$$

$$ER = 10^{-9} \times \rho_w \cdot K(\alpha\, Hv)^{k_1 b}\left(\frac{V}{v_{ref}}\right)^{k_2}\left(\frac{d_p}{d_{ref}}\right)^{k_3} g(\theta) \tag{7.}$$

$$k_2 = 2.3(HV)^{0.038}, \qquad HB = \frac{HV + 0.1023}{0.0108} \tag{8.}$$

The ER (kg/kg) is defined as the mass of removed material from the sample divided by the mass of erodent impacting the surface. ρ_w and HV (GPa) are the density and Vickers hardness of the target material, respectively. d_{ref} and v_{ref} are the reference particle diameter (326 μm) and the velocity (104 m/s) of the particle, respectively. k_2 is the particle impact velocity exponent, k_3 is determined by the properties of the particle. The detailed parameters are listed in Table 3.

The impact angle function $g(\theta)$ is defined by:

$$g(\theta) = (sin\theta)^{n_1}(1 + HV(1 - sin\theta))^{n_2} \tag{9.}$$

$$n_1 = 0.71(HV)^{0.14}, \qquad n_2 = 2.4(HV)^{-0.94} \tag{10.}$$

where n_1 and n_2 are determined by the particle properties and the eroded material hardness. The impact angle function $g(\theta)$ of SiO_2~QBe_2 is shown in Fig. 2.

Furthermore, in the present a user defined function (UDF) code is developed into the ANSYS FLUENT software to calculate the erosion depth and total mass loss:

$$\Delta W = \mathrm{ER} \cdot m_i \cdot t \times 1000, \qquad \Delta h_i = \frac{ER_i \cdot m_i \cdot t}{\rho_w \cdot A_i} \times 1000 \tag{11.}$$

where Δh_i (mm) and Δw (g) are the erosion depth and total mass loss, respectively. t (s) is the test time. m_i (kg/s) is the mass rate of particles impacting the computational cell area A_i (m_2).

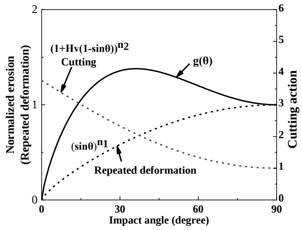

Fig. 2 The erosion arising from repeated plastic deformation and cutting action according to Eq. (9)-(10)

DOI: 10.36547/ams.27.1.851

Table 3 Parameters for Oka erosion model

Material type	QBe_2 (C17200)	Model constant, n_2	1.14
Particle type	Angular SiO2	Velocity exponent	2.37
Reference erosion rate	0.0006026	Diameter exponent	0.19
Wall material Vickers (GPa)	2.2	Reference diameter (m)	0.000326
Model constant, n_1	0.79	Reference velocity (m/s)	104

3.3. Computational mesh and geometry

Fig. 3 shows the simplified geometry and the mesh used in the CFD simulation. Three kind of meshes as shown in Fig.4 were created by ICEM to conduct the mesh refinement study, with a refinement ratio of 1.5.

The grid convergence method proposed by Roache [24] is used to analyze the uncertainty of the upstream average erosion rate caused by the grid refinement in Table 4. To obtain representative average velocity and turbulence fluctuations value of particle interaction in the near-wall cell, it is recommended to set the thickness of the first layer equal to the particle size [25-27]. The convergence index for coarse and intermediate meshes is 4.8% while intermediate and finer meshes is 0.84%. Meanwhile, the asymptotic range of convergence is 0.97 and the order of grid convergence is 4.39. As it can be seen, the intermediate mesh is sufficient to meet the simulation accuracy requirements.

Table 4 Parameters setting of grid refinement study (Realizable κ-ε model)

Mesh group	Refinement ratio	The number of elements	Average erosion rate (kg/m^2·s)
Mesh 1	1	68640	5.96×10^{-6}
Mesh 2	1.5	220320	5.01×10^{-6}
Mesh 3	2.25	717810	4.85×10^{-6}

3.3. Boundary conditions and numerical schemes

ANSYS FLUENT 2019 was used for numerical simulations. For complex flow problems involving pressure gradient and impact, non-equilibrium wall functions are recommended [28]. The boundary conditions adopt velocity inlet and pressure outlet. The turbulence specification method was used taking into account the turbulence intensity (5%) and hydraulic diameter (0.083 m). The Couple-Pseudo transient algorithm was used to solve the pressure-velocity coupling problem and QUICK discretization scheme was used to determine the momentum, the convection and divergence terms, and the PRESTO for the pressure term.

As the particle concentration is low, one-way coupling can be employed. The Rosin-Rammler model [29] is used to calculate the particle distribution. The average particle diameter is estimated as 0.000181 m, the particle distribution exponent is 2.5 and the non-spherical coefficient is 0.8.

RESULTS AND DISCUSSION

4.1. Turbulence model analysis

Different types of turbulence models will lead to different turbulence scales, which will lead to differences in particle trajectory prediction. In this study, three turbulence models of Realizable κ-ε, SST κ-ω and RSM are used to analyze the erosion rate of MWD barrel [30]. The experimental data from Test 1 was used to determine which model performed best in predicting the overall erosion profile.

As can be seen from Table 5, the total mass loss of RSM model and SST κ-ω model is close to the experiment values, while the Realizable κ-ε model is obviously over-predictive in the downstream of MWD. The significant erosion localization is found by the SST κ-ω model and RSM model in Fig. 5(b) and (c), but the experimental erosion profile is dispersed and randomly distributed. In comparison with the experimental data, the erosion depth and erosion profile predicted by the SST κ-ω model and RSM model are not as good as that by Realizable κ-ε model in Fig. 5(a) and Fig. 6. Therefore, the Realizable κ-ε model is selected as turbulence model for the CFD simulation.

Table 5 Comparison of total mass loss with different turbulence models

Conditions	Realizable κ-ε (g)	SST κ-ω (g)	RSM (g)	Experiment (g)
Test1	81.35	45.36	47.53	57.23
Test2	21.18	11.08	11.25	23.28
Test3	7.6	4.19	4.32	14.52

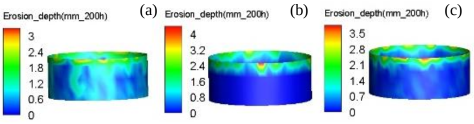

Fig. 5 Contours of erosion depth with different turbulence models (Test1): (a) Realizable κ-ε, (b) SST κ-ω, and (c) RSM

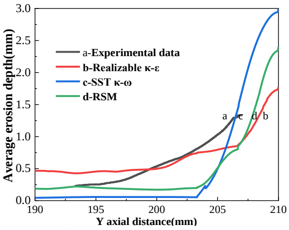

Fig. 6 Comparison of average erosion depth with different turbulence models (Test1)

4.2. Comparison between CFD simulation and experimental results

A combination of CFD calculation and experimental results is conducted to study the influence of fluid flow on the slurry erosion process and erosion mechanism. Under different fluid flows, the erosion distribution of MWD barrel by the simulation and experimental results is shown in Fig. 7. The erosion wear is mainly distributed in the upstream of MWD barrel.

Since the MWD barrel is not a plane, there is a curvature error in the radial direction. In the experiment measurements, it is noted that the erosion profile is distributed randomly. In order to reduce the measurement error, the multiple line data in the Y-axis direction are extracted and averaged. For Test 1, the erosion wear is mainly distributed in the range of 200-210 mm. Generally the trend of erosion wear decreased gradually from the top to the bottom in the upstream of MWD barrel. CFD simulation can well predict the erosion profile, and the predicted erosion depth is relatively consistent with the experimental data as shown in Fig. 7(a) and Fig. 6. Under high pressure and high fluid flow (Test 2), the interaction between particle erosion and pressure, the area of slurry erosion is expanded and the erosion depth is increased in Fig. 7(b) and Fig. 8. In the range of 205-210 mm, CFD can better predict the erosion depth, which is agreement with the experimental measurement. When Von Mises stress becomes larger in the range of 190-200 mm, plastic deformation caused by high pressure dominates, and it is difficult for the existing erosion model to predict complex conditions as shown in Fig. 8 [31, 32]. For Test 3, the erosion wear are negligible in comparison with the experimental measurement. Surface damage may be caused by plastic deformation due to high pressure, resulting in a uniform concave in the middle and convex on both sides in the upstream of MWD barrel in Fig. 7(c).

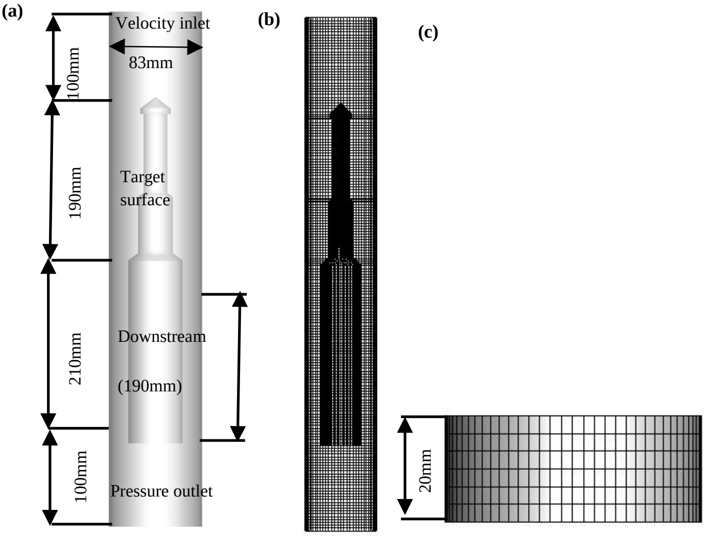

Fig. 3 Geometry and mesh of MWD barrel. (a) geometry, (b) computational domain, (c) upstream

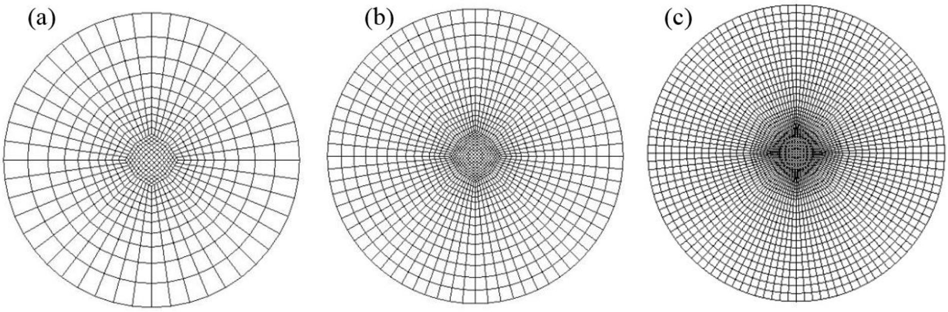

Fig. 4 Different density of mesh on the cross-section. (a) Coarse mesh, (b) Intermediate mesh, (a) Fine mesh

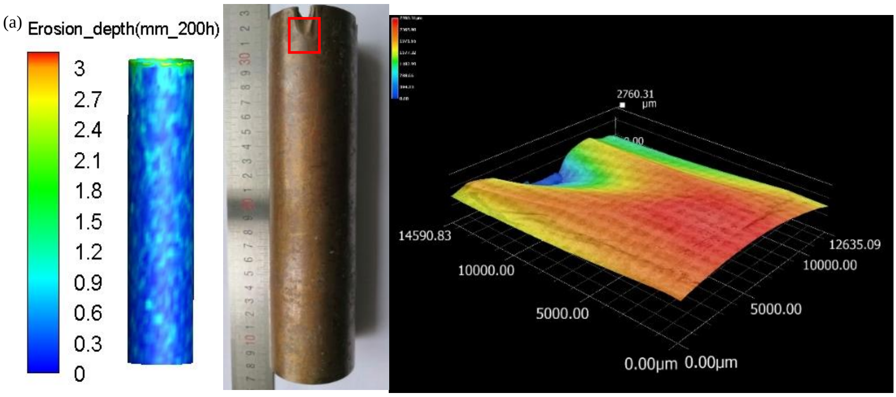

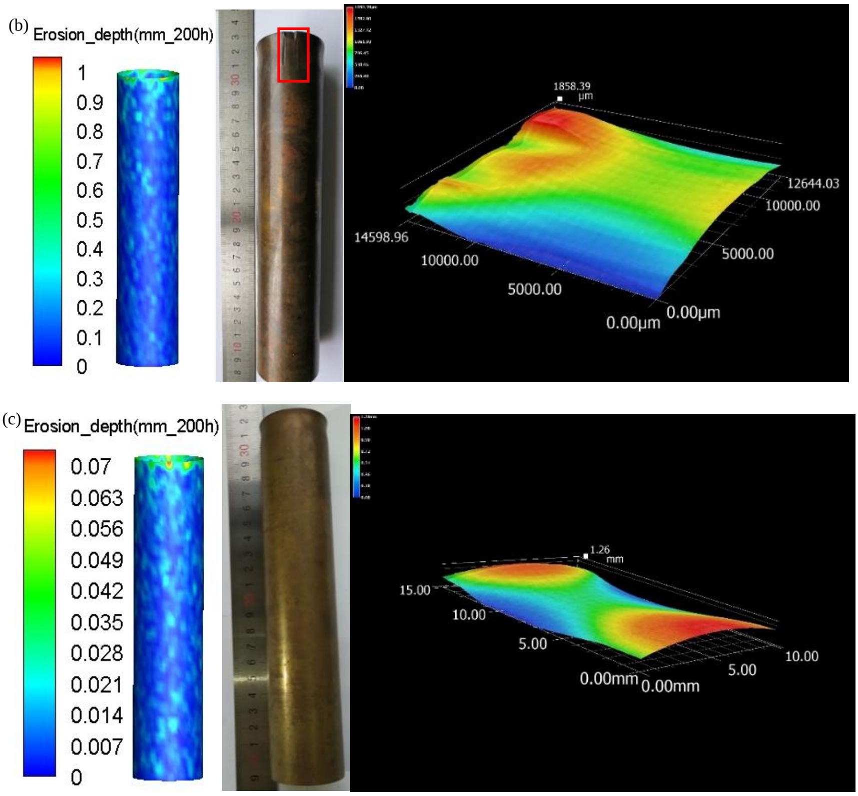

Fig. 7 Comparison between the actual erosion wear and the CFD predictions. (a) Test 1, (b) Test 2, (c) Test 3

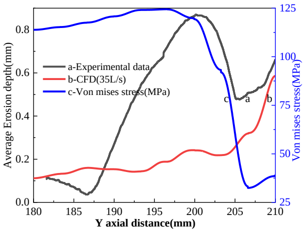

Fig. 8 Comparison of the average erosion depth and Von Mises stress with actual erosion (Test 2)

To further understand the erosion process and erosion mechanism, the surface morphology of MWD barrel after erosion is observed by Super Depth 3D microscope. The erosion morphology is mainly affected by the particle impact velocity, particle impact angle and Von Mises stress. Figure 9 shows the contours of erosion-related variables (such as erosion depth, particle impact velocity, particle impact angle and sand mass per unit area) under different fluid flow. It can be seen that the fluid flow has a certain degree of influence on the shape of the erosion scar. As the particle velocity decreases, the ability of fluid flow to carry particles becomes stronger, and more particles will impact the surface of MWD barrel in the upstream with the fluid, and the impact angle will increase. Therefore, the combination of CFD simulation and experimental approach can be used to identify and explain the slurry erosion mechanism in different regions.

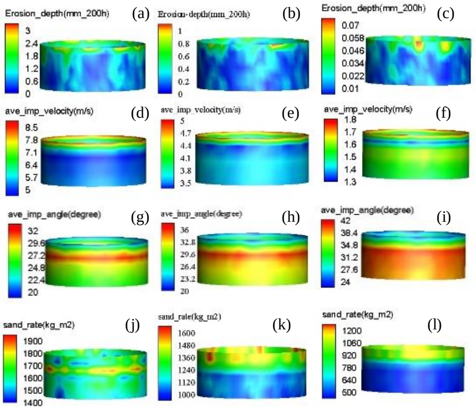

Fig. 9 Contours of erosion-related variables (including erosion depth, particle impact velocity, particle impact angle and sand mass per unit area) with different fluid flow: Test 1 (a, d, g and j), Test 2 (b, e, h and k), Test 3 (c, f, i and l)

Under high fluid flow (Test 1), small fragments were induced by the repeated cutting actions of high-velocity particles at low impact angle. These fragments were washed away by the incoming slurry and subsequently removed from the material surface, resulting in scratches and vulnerable lip formation [33,34] as shown in Fig. 10(a) and (b). Under high pressure and high fluid flow (Test 2), the impact force of the particles becomes bigger, the pits form on the surface and are becoming larger and deeper in Fig. 10(c) and (d). In the middle of the upstream (195-200 mm), the Von Mises stress and particle impact angle become bigger, plastic deformation and cracks caused by indentation dominate in Fig. 10 (e) and (f) [34-36]. Under high pressure and low fluid flow (Test 3), the particle impact velocity is relatively low, but the impact angle increases. The micro-pits and scratches form, resulting in a large number of micro-pits and scratches in Fig. 10(g) and (h). These slurry erosion characteristics are very similar to the experimental study of slurry erosion results [34].

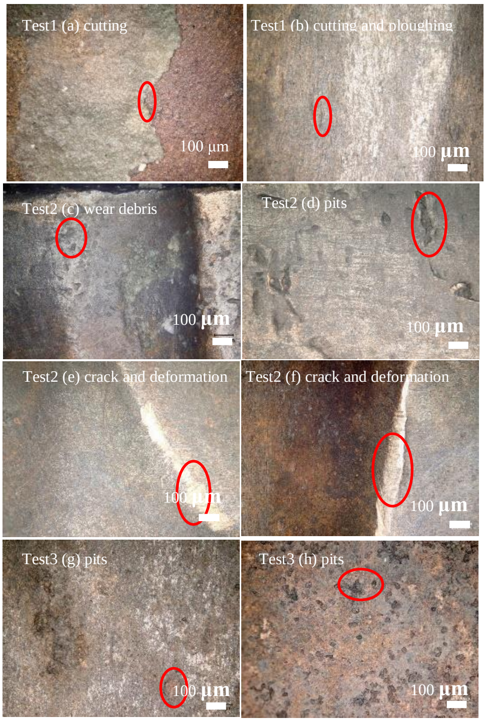

Fig. 10 Surface morphologies in different regions of MWD barrel. (I) in the top of upstream (205-210mm): (a), (c), (d) and (g), (II) in the middle of upstream (195-200mm): (b), (e), (f) and (h)

CONCLUSIONS

1) The SST κ-ω and the RSM model predictions are insufficient in particle-fluid interaction, showing the obvious erosion localization in the upstream of MWD barrel. The realizable κ-ε model can well predict the erosion profile and the erosion depth is consistent with the experiment results.
2) Under high fluid flow, particle erosion wear is mainly distributed in the range of 200 ~ 210 mm, and the overall trend gradually decreases from the top to the bottom of MWD barrel; under high pressure and high fluid flow, particle erosion and pressure interaction further expand the area and the depth of slurry erosion; under high pressure and low fluid flow, the particle erosion is negligible, and plastic deformation caused by high pressure is dominant.
3) A user defined function (UDF) code is developed to calculate the particle characteristics to understand the slurry erosion process and explain the erosion mechanisms. The impact of particles at high velocity and low angle is dominated by the cutting mechanism. Under high angle and high Von Mises stress, plastic deformation caused by indentation is dominated; for high velocity of particles, large pits and cracks are formed, and micro-pits and scratches form at low velocity particles.

ACKNOWLEDGMENTS

The authors are grateful to be supported by the Priority Academic Program Development of Jiangsu Higher Education Institutions (PAPD), the Top-notch Academic Programs Project of Jiangsu Higher Education Institutions (TAPP), and the Science and Technology Project of Changzhou, P. R. China under grant No.CZ20180016 and CE20170028.

REFERENCES

1. J. Zhao, G. Zhang, Y. Xu: Powder Technol., 313, 2017, 231-244.
http://doi.org/10.1016/j.powtec.2017.03.026.

2. F. Wang, R. Wang, W. Zhou: Int. J. Impact Eng., 102, 2017, 169-179.
https://doi.org/10.1016/j.ijimpeng.2016.12.019.

3. M. Parsi, K. Najmi, F. Najafifard, S. Hassani, B.S. McLaury, S.A. Shirazi: J. Nat. Gas. Sci. Eng., 21, 2014, 850-873.
http://doi.org/10.1016/j.jngse.2014.10.001.

4. G.C. Pereira, F.J. de Souza, D.A. de Moro Martins: Powder Technol., 261, 2014, 105-17.
http://doi.org/10.1016/j.powtec.2014.04.033.

5. A. Mansouri, H. Arabnejad, S.A. Shirazi, B.S. McLaury: Wear, 332-333, 2015, 1090-1097.
http://doi.org/10.1016/j.wear.2014.11.025.

6. I.M. Hutchings: Wear, 70, 1981, 269-281.
https://doi.org/10.1016/0043-1648(81)90347-1.

7. M.A. Islam, Z.N. Farhat: Wear, 311, 2014, 180-190.
http://doi.org/10.1016/j.wear.2014.01.005.

8. Q.B. Nguyen, C.Y.H. Lim, V.B. Nguyen, Y.M. Wan, B. Nai, Y.W. Zhang, M. Gupta: Tribol. Int., 79, 2014, 1-7.
http://doi.org/10.1016/j.triboint.2014.05.014.

9. I. Finnie: Wear, 186-187, 1995, 1-10.
http://doi.org/10.1016/j.triboint.2014.05.014.

10. M. Lindgren, J. Perolainen: Wear, 321, 2014, 64-69.
http://doi.org/10.1016/j.wear.2014.10.005.

11. H.S. Grewal, H. Singh, E.-S. Yoon: Wear, 332-333, 2015, 1111-1119.
http://doi.org/10.1016/j.wear.2015.02.039.

12. C.Y. Wong, C. Solnordal, L. Graham, G. Short, J. Wu: wear, 336-337, 2015, 72-85.
http://doi.org/10.1016/j.wear.2015.04.020.

13. D.N. Veritas: Recommended practice RP O501 erosive wear in piping systems, 2007. http://shaghool.ir/files/erosive-wear-in-piping-systems-rp-o501.pdf.

14. Y. Zhang, E.P. Reuterfors, B.S. McLaury, S.A. Shirazi, E.F. Rybicki: Wear, 263, 2007, 330-338.
http://doi.org/10.1016/j.wear.2006.12.048.

15. Y.I. Oka, K. Okamura, T. Yoshida: Wear, 259, 2005, 95-101.

http://doi.org/10.1016/j.wear.2005.01.039.
16. Y.I. Oka, T. Yoshida: Wear, 259, 2005, 102-109. http://doi.org/10.1016/j.wear.2005.01.040.
17. G. Grant, W. Tabakoff: J. Aircraft., 12, 1975, 471-478. https://doi.org/10.2514/3.59826.
18. R.E. Vieira, A. Mansouri, B.S. McLaury, S.A. Shirazi: Powder Technol., 288, 2016, 339-353. http://doi.org/10.1016/j.powtec.2015.11.028.
19. W. Peng, X. Cao: Powder Technol., 294, 2016, 266-279. http://doi.org/10.1016/j.powtec.2016.02.030.
20. M. Agrawal, S. Khanna, A. Kopliku, T. Lockett: Wear, 426-427, 2019, 596-604. https://doi.org/10.1016/j.wear.2019.01.018.
21. A. Mansouri: *A combined CFD-experimental method for developing an erosion equation for both gas-sand and liquid-sand flows*, The University of Tulsa, 2016.
22. A. Haider, O. Levenspiel: Powder Technol., 58, 1989, 63-70. https://doi.org/10.1016/0032-5910(89)80008-7.
23. A. Forder, M. Thew, D. Harrison: Wear 216, 1998, 184-193. https://doi.org/10.1016/S0043-1648(97)00217-2.
24. P. J. Roache, K. N. Ghia, F. M. White: J. Fluids Eng., 108 1986, 2. http://doi.org/10.1115/1.3242537.
25. F. Najafifard: *Predicting near wall particle behavior with application to erosion simulation*, The University of Tulsa, 2014.
26. T. A. Sedrez, S. A. Shirazi, Y. R. Rajkumar: Wear 426 2019, 570-580. https://doi.org/10.1016/j.wear.2019.01.015.
27. A. Mansouri, H. Arabnejad, S. Karimi, S.A. Shirazi, B.S. McLaury: Wear, 338-339, 2015, 339-350. http://dx.doi.org/10.1016/j.wear.2015.07.011.
28. J. Zhang, F. Darihaki, S.A. Shirazi: Wear, 430-431, 2019, 191-201. https://doi.org/10.1016/j.wear.2019.04.029.
29. P. Rosin: J. Fluids Eng., 7, 1933, 29-36.
30. J. Zhang, B.S. McLaury, S.A. Shirazi: Wear, 394-395, 2018, 11-19. http://doi.org/10.1016/j.wear.2017.10.001.
31. H. Wang, Y. Yu, J. Yu, Z. Wang, H. Li: Tribol. Int., 137, 2019, 387-404. https://doi.org/10.1016/j.triboint.2019.05.019.
32. H. Wang, Y. Yu, J. Yu, W. Xu, X. Li, S. Yu: Wear, 440-441, 2019, 203043. https://doi.org/10.1016/j.wear.2019.203043.
33. T. Alam, Z.N. Farhat: Eng. Fail. Anal., 90, 2018, 116-128. https://doi.org/10.1016/j.engfailanal.2018.03.019.
34. B. Sun, J. C. Fan, D. Wen: Tribol. Int., 82, 2015, 280-286. http://dx.doi.org/10.1016/j.triboint.2014.07.025.
35. R. Bidulsky,M. Actis Grande, E. Dudrova, M. Kabatova, J. Bidulska: Powder Metall., 59(2), 2016,121-127 https://doi.org/10.1179/1743290115Y.0000000022.
36. J.Bidulská, R. Bidulský, M.A. Grande, T. Kvačkaj: Materials, 12(22), 2019, 3724. https://doi.org/10.3390/ma12223724.